SCALING AND SEISMIC REFLECTIVITY: IMPLICATIONS OF SCALING ON AVO

Felix J. Herrmann

Earth Resources Laboratory
Department of Earth, Atmospheric, and Planetary Sciences
Massachusetts Institute of Technology
Cambridge, MA 02139

ABSTRACT

AVO analysis of seismic data is based on the assumption that transitions in the earth consist of jump discontinuities only. The generalization of this type of transition to a more realistic class of transitions shows a drastic change in observed AVO behavior, especially for the large angles currently attained by increasing cable lengths. We propose a simple approach that accounts for this anomalous behavior by renormalizing the observed AVO. This renormalization allows for a separation of the observed AVO effects in terms of a conventional Zoeppritz contribution and a scaling contribution in those cases where the transitions can no longer be considered as isolated jump discontinuities. After renormalization, the inverted fluctuations regain their relative magnitudes which, due to the scaling, may have been significantly distorted. An example of these distortions are tuning effects, often erroneously interpreted as bright spots.

INTRODUCTION

Observed amplitude-variation-with-offset (AVO) behavior of surface seismic reflection data has led to inferences ranging from the successful identification of hydro-carbon traps (Castagna and Backus, 1993) to the misidentification of AVO anomalies. The reason for this mixed success does not necessarily lie in the data's intricacies but may be caused by oversimplification of the models, and the lack of understanding of both the reflection and propagation characteristics of seismic waves. Recent increases in cable lengths are making these matters even worse. Amongst the various identifiable issues that are responsible, one may mention the current inability to accurately model seismic amplitudes, successfully integrate well and seismic data, and unambiguously interpret AVO.

By limiting the focus to reflectivity in one-dimensional loss-less elastic media, we aim to provide new insights in describing observed anomalous AVO behavior, caused by effects other than anelasticity or multi-dimensionality of the medium. Instead, we study effects related to thin bed-tuning/fine-layering. Contrary to Swan (1991) and Wapenaar *et al.* (1999), the anomalies are not being considered as artifacts but rather as direct consequences of natural extensions of the expected behavior in cases where the assumptions underlying the theory no longer seem to be justified. Multiscale scale analysis (Mallat and Hwang, 1992; Bacry *et al.*, 1993; Holschneider, 1995; Herrmann, 1997; Dessing, 1997) on well data serves as the primary motivation for this approach, since it suggests the presence of a much broader class of transitions of which the prevailing reflector model, the jump discontinuity, is only one particular instance (Herrmann, 1997, 1998b). In effect, multiscale analysis clearly shows that well data (Muller *et al.*, 1992; Saucier and Muller, 1993; Saucier *et al.*, 1997; Herrmann, 1997, 1998a) show evidence of a highly complex multifractal behavior (Bacry *et al.*, 1993; Jaffard, 1997a,b), which corresponds to both an accumulation of the transitions as well as wildly varying of their order with position.

Recent approaches by Swan (1991, 1997), Wapenaar *et al.* (1999), and much earlier by Payton (1977) address tuning anomalies, which are expected to arise in these highly complex multifractal media. Their point of view is that the observed AVO and seismic signatures are caused by interferences, induced by a multitude of thin layers. In this paper, a different approach is taken. Instead of dealing with the problem on the level of fine-layering, a complementary possibility is explored that addresses the complexity issue at the coarse seismic scale. By allowing transitions at that length scale to become more general than jump discontinuities, an intrinsic scale dependence of the medium variations is introduced. This scale dependence, absent in conventional approaches, allows for an effective characterization of the local complexity by means of fractional-order onset functions (Holschneider, 1995; Dessing, 1997; Herrmann, 1997). Consequently, the scale dependence gives rise to an AVO behavior now consisting of an intermingling of the traditional intrinsic contribution and a new scaling contribution. The first approximately equals the well-known angle dependent term in the linearized Zoeppritz formulation (Aki and Richards, 1980; van Wijngaarden, 1998), while the second involves a contribution from the scale dependent fluctuation. The latter contribution is an immediate consequence of the correspondence between the off-set dependent stretching and differentiation within the imaged reflectivity, and the dilations and differentiations within the continuous wavelet transform. Both the wavelet coefficients (Holschneider, 1995; Dessing, 1997; Herrmann, 1997; Mallat, 1997) and reflectivity measure the scaling of the transitions. Given this scale contribution, tuning effects are easily explained by scaling and more importantly, these scaling effects are accounted within the inversion process, yielding more accurate results.

In a recent paper, Wapenaar *et al.* (1999) propose to filter AVO data to remove the effect of scaling. They design a filter that ensures the vertical wavelength to remain constant as a function of the off-set. Even though scaling effects are removed in this way,

their method suffers from the fact that it goes at the expense of reducing the resolution to that of the maximum wavelength. Given the increasing cable lengths this filtering is not really an option. Instead, my method utilizes information on the local scaling of the reflector. Information on the local scaling is captured directly from data by the monoscale analysis method (Herrmann and Startk, 1999, 2000; Stark and Herrmann, 2000), and is subsequently used to correct for the scaling contribution. The monoscale analysis (Herrmann and Stark, 1999, 2000; Stark and Herrmann, 2000) measures, within the seismic bandwidth, the sharpness of the generalized transitions by means of a scaling exponent. To the order of magnitude these scale exponents describe the sharpness and local scaling of the generalized transitions and provide adequate information to renormalize the measured AVO as to account for scaling effects within Zoeppritz inversion.

In this paper, we give a brief overview of the seismic reflectivity imaging method involving a one-way representation of the seismic wavefield, the formulation of the imaging principle for migration, and the derivation of a linearized Zoeppritz convolution model for the imaged reflectivity. This exposition is followed by a short introduction to multiscale analysis by the continuous wavelet transform. Zero-order jump discontinuities are generalized to varying order transitions whose order uniquely determines the sharpness and the scaling of the wavelet coefficients. After establishing the existence of a fundamental link between the wavelet transform and pre-stack imaged reflectivity, ample attention is paid to what goes wrong when reflectors are no longer limited to jump discontinuities at the seismic scale. For a jump discontinuity the wavelet coefficients are conveniently scale-independent, whereas nonzero order transitions definitely display a distinct scale dependence. Next, we discuss the implication of this scale dependence on AVO behavior. It is argued that varying the off-set results in varying the dominant vertical wavelength. This vertical wavelength is proportional to the scale. Consequently, depending on the transition's order the scale contribution to the AVO may be of the same order as the intrinsic AVO. We obtain information on the order of the transitions by conducting monoscale analysis on the reflection gather or on the post-stack migrated data. This information is used to renormalize the anomalous AVO behavior by applying a scale correction. The study concludes with a series of numerical experiments illustrating the value of the proposed method.

SEISMIC REFLECTIVITY IMAGING METHOD

Medium variations of the earth's upper crust sedimentation and mantle exhibit distinct directional preference along the vertical. Therefore, it is beneficial to reformulate the omni-directional two-way wave equation into a wave equation which distinguishes between up- and downward traveling waves. As a consequence of this choice, natural separation can be made between propagation and reflection of seismic waves (Berkhout, 1987; Wapenaar and Berkhout, 1989; de Hoop, 1992). For laterally slowly varying media, propagation effects are predominantly determined by the integrated local vertical

slowness structure. Reflectivity, on the other hand, is mainly governed by local vertical variations in the medium. By assuming the earth to vary weakly along the vertical only, a simple formulation for the migrated reflectivity can be derived. The obtained expressions are linear in the medium variations as well as of the convolutional type.

One-Way Wavefield Representation

Following Berkhout (1987), Wapenaar and Berkhout (1989), Wapenaar (1996), Grimbergen *et al.* (1998), de Hoop (1992, 1998), and Wapenaar *et al.* (1999), one can write, for a lateral homogeneous elastic medium, an up-going plane wave[1] in the temporal frequency ray-parameter (p, ω)-domain as

$$P_{i,j}(\mathrm{p}, z_0; \omega) = \int_{z_0}^{\infty} W_i^-(\mathrm{p}, z_0, z; \omega) R_{i,j}(\mathrm{p}, z) W_j^+(\mathrm{p}, z, z_0; \omega) S_j(\omega) \mathrm{d}z. \tag{1}$$

In this formulation:

Each of the subscripts i, j stand for the two[2] wave types under consideration, the compressional or shear.

z, p and ω are respectively, the vertical coordinate, the i-mode ray-parameter, $\mathrm{p} = \frac{\sin\theta_i}{c_i}$ and the temporal angular frequency, $\omega = 2\pi f$.

$P_{i,j}^-$'s are the decomposed multi-component reflected data for waves traveling in the i or j mode.

W_i^+ and W_j^- are the propagation operators given by

$$W_j^+(\mathrm{p}, z, z_0; \omega) = W_j^-(\mathrm{p}, z, z_0; \omega) = \exp(j\omega\bar{q}_i(\mathrm{p})(z - z_0)), \tag{2}$$

where $\bar{q}_i(\mathrm{p}) = \sqrt{\frac{1}{\bar{c}_i^2} - \mathrm{p}^2}$ is the vertical slownesses of the background velocity model given by either the compressional or shear wavespeed c_i.

$R_{i,j}$ is the reflection density.

S_j is the j type omni-directional temporal one-way source distribution.

The above expression is approximate since it is formulated in terms of a homogeneous velocity model as denoted by the barred quantities. Extension toward a slowly varying background model is possible when fluctuations are small or take place on a length scale much larger than that of the dominant wavelength.

Equation 1 forms the basis of subsequent series of simplifications which will be discussed next. These simplifications lead to a representation of the imaged reflectivity in

[1]The wavefields may include all multiple reflections, mode conversions and even dispersion effects while the formalism readily extends itself to lateral varying media.

[2]SH-waves are not considered here since they behave essentially the same as scalar acoustic waves.

terms of a simple spatial convolution model. To arrive at this result the wave propagation is assumed to be without dispersion, while the mode conversions are limited to conversions during the reflection[3] only.

Migration

From the one-way plane wave formalism presented in equation 1, one can derive an expression for the imaged angle dependent reflectivity by imposing the imaging condition on the downward extrapolated wavefield (Claerbout (1971). Following Wapenaar *et al.* (1999) this expression can be written in the form

$$\langle R_{i,j}(\mathrm{p},z)\rangle = \frac{\bar{\sigma}_{i,j}(\mathrm{p})}{\pi}\Re\int P_{i,j}(\mathrm{p},z;\omega)\mathrm{d}\omega, \tag{3}$$

where $P_{i,j}(\mathrm{p},z;\omega)$ is the downward extrapolated wavefield given by de Hoop (1998)

$$P_{i,j}(\mathrm{p},z;\omega) = (TW_i^-(z_0,z;\omega))P_{i,j}(\mathrm{p},z_0;\omega)(TW_j^+(z,z_0;\omega)). \tag{4}$$

The p-dependent factor, $\bar{\sigma}_{i,j}(\mathrm{p})$, will be defined below and is there for dimensionality purposes[4]. The action of the time reversal operator is given by, $(Tf)(t) = f(-t)$. The brackets $\langle\rangle$ are used to denote the imaged reflectivity, which still contains the source contribution. Equations 3 and 4 are applied recursively while stepping down from the surface into the subsurface.

Convolution Model for Migrated Reflectivity

For a homogeneous medium the imaged reflectivity (cf. equation 3) can be written as a spatial convolution. Substitution of equation 3 into the one-way wave representation (cf. equation 1) yields, after setting z_0 to $z_0 = 0$,

$$\langle R_{i,j}(\mathrm{p},z)\rangle = \frac{\bar{\sigma}_{i,j}(\mathrm{p})}{\pi}(r_{i,j} *_z s)(\mathrm{p},z). \tag{5}$$

In this expression the source function $s(\mathrm{p},z)$ is given by

$$s(\mathrm{p},z) = \mathcal{F}^{-1}\{\bar{\sigma}_{i,j}(\mathrm{p})S(\omega\bar{\sigma}_{i,j}(\mathrm{p}))\}(z) = s(\frac{z}{\bar{\sigma}_{i,j}(\mathrm{p})}) \tag{6}$$

with $\mathcal{F}\{\cdot\}(z)$ the inverse spatial Fourier transform and

$$\bar{\sigma}_{i,j}^{-1}(\mathrm{p}) = \bar{q}_i(\mathrm{p}) + \bar{q}_j(\mathrm{p}). \tag{7}$$

Equation 6 corresponds to a p-dependent rescaling of the temporal source wavelet. Expressions for the pointwise reflection density itself, $r_{i,j}(\mathrm{p})$, are derived from the decomposition and composition matrices. (For details see Aki and Richards, 1980; Wapenaar and Berkhout, 1989; de Hoop, 1992; van Wijngaarden, 1998.)

[3]Burridge and Chang (1989) showed that in finely layered media only the PP and SS transmission effects matter, i.e. Albeigh waves may be mode converted along their path; only waves going in as P or S and leaving as P and S significantly contribute.

[4]The dimensionality argument is related to the fact that the plane wave imaged reflectivity is a density in both the vertical and ray-parameter dimensions.

Linearization for PP-Reflectivity

We study PP reflections for acoustic and elastic media. Simplified expressions for the reflection density are obtained by linearizing the reflection density in terms of small normalized perturbations in the acoustic impedance, shear modulus, and density. This linearization leads to the following comprehensive expression for the PP reflection density (Castagna and Backus, 1993; Ostrander, 1994; van Wijngaarden, 1998)

$$r_{pp}(\mathrm{p},z) \approx \frac{1}{2}\frac{\mathrm{d}}{\mathrm{d}z}\Delta Z + \frac{1}{2}\left(\frac{\bar{c}_p^2\mathrm{p}^2}{\cos^2\bar{\theta}_p}\right)\frac{\mathrm{d}}{\mathrm{d}z}\Delta c_p - 2\bar{c}_s^2\mathrm{p}^2\frac{\mathrm{d}}{\mathrm{d}z}\Delta\mu \tag{8}$$

with

$$\frac{\mathrm{d}}{\mathrm{d}z}\Delta Z = \frac{\mathrm{d}}{\mathrm{d}z}\Delta c_p + \frac{\mathrm{d}}{\mathrm{d}z}\Delta\rho \quad \text{and} \quad \frac{\mathrm{d}}{\mathrm{d}z}\Delta\mu = \frac{\mathrm{d}}{\mathrm{d}z}2\Delta c_s + \frac{\mathrm{d}}{\mathrm{d}z}\Delta\rho, \tag{9}$$

for the normalized fluctuations in the acoustic impedance, Z and shear modulus, μ. The density is denoted by ρ. For an arbitrary quantity $f(z)$, the normalized fluctuations, $\Delta f(z)$, are defined as the difference between the actual and background medium, normalized by the background, i.e. $\Delta f(z) \triangleq \frac{\delta f}{\bar{f}}(z)$ where $\delta f(z) \triangleq f(z) - \bar{f}$. Equations 8 and 9 are accurate when the background is chosen such that for all medium properties $\Delta f(z) \triangleq \frac{\delta f}{\bar{f}}(z) \ll 1$. Finally, the cosine in the second term of equation 8 is given by

$$\cos\bar{\theta}_p = \sqrt{1 - \bar{c}_p^2\mathrm{p}^2}. \tag{10}$$

Using vector notation, equation 8 can be written in terms of a matrix vector multiplication, yielding the following formulation for the linearized down- and upgoing PP reflection densities,

$$\begin{pmatrix} r_{pp}^{+} \\ r_{pp}^{-} \end{pmatrix}(\mathrm{p},z) = \begin{pmatrix} +\frac{1}{2} & +\frac{1}{2}\frac{\bar{c}_p^2\mathrm{p}^2}{\cos\bar{\theta}_p(\mathrm{p})} & -2\bar{c}_s^2\mathrm{p}^2 \\ -\frac{1}{2} & -\frac{1}{2}\frac{\bar{c}_p^2\mathrm{p}^2}{\cos\bar{\theta}_p(\mathrm{p})} & +2\bar{c}_s^2\mathrm{p}^2 \end{pmatrix} \partial_z \begin{pmatrix} \Delta Z \\ \Delta c_p \\ \Delta\mu \end{pmatrix}(z) \tag{11}$$

$$= \bar{\mathbf{M}}(\mathrm{p},x)\partial_z\boldsymbol{\Delta}(z). \tag{12}$$

All p dependent terms are incorporated in the matrix $\bar{\mathbf{M}}(\mathrm{p},x)$, while vector $\boldsymbol{\Delta}(z)$ contains contributions from the normalized medium fluctuations.

Imaged Linearized PP-Reflectivity

Combining equations 11–12 with the expression for imaged reflectivity (cf. equation 5) gives, with a slight abuse of notation,

$$\langle R_{pp}(\mathrm{p},z)\rangle \approx \bar{\mathbf{M}}(\mathrm{p})\frac{\bar{\sigma}_{i,j}(\mathrm{p})}{\pi}(\partial_z\boldsymbol{\Delta} * s)(\mathrm{p},z), \tag{13}$$

which can, using equation 6, be rewritten into the form

$$\langle R_{pp}(\mathrm{p},z)\rangle \approx \bar{\mathrm{M}}(\mathrm{p})\frac{\bar{\sigma}_{i,j}(\mathrm{p})}{\pi}\frac{\mathrm{d}}{\mathrm{d}z}(\boldsymbol{\Delta} * s_\sigma)(z) \tag{14}$$

with

$$s_\sigma(z) = s(\frac{z}{\bar{\sigma}_{pp}(\mathrm{p})}) = s(\frac{2\cos\bar{\theta}_p}{\bar{c}_p}z) \quad \text{and} \quad \bar{\sigma}_{pp}^{-1}(\mathrm{p}) = 2\sqrt{\frac{1}{\bar{c}_p^2}-\mathrm{p}^2} = 2\frac{\cos\bar{\theta}_p}{\bar{c}_p}. \tag{15}$$

Due to the p-dependent stretchings of the wavelet, distinctions between the angle (p)-dependent and fluctuation (Δ)-dependent parts (cf. equation 8) can no longer be made for the imaged reflectivity. Only when the medium contains well-isolated jump discontinuities can the separation accomplished again.

IMAGED SEISMIC REFLECTIVITY VERSUS THE WAVELET TRANSFORM

Expressions for the PP imaged reflectivity can be linked directly to a specific instance of the continuous wavelet transform. Consequences of this fundamental observation will be discussed in detail.

The Continuous Wavelet Transform

The continuous wavelet transform of a function f is given by

$$\mathcal{W}\{f,\psi^M\}(\sigma,z) \triangleq \sigma^M\frac{\mathrm{d}^M}{\mathrm{d}z^M}(f * \phi_\sigma)(z), \tag{16}$$

where ϕ_σ is a sufficiently smooth ($2M$-times differentiable) smoothing function with support σ. ψ_σ^M is a wavelet generated by dilations of $\psi^M(z) = (-1)^M\frac{\mathrm{d}^M}{\mathrm{d}x^M}\phi(z)$. M rules the number of vanishing moments, i.e.

$$\int_{-\infty}^{+\infty} z^m\psi^M(z)\mathrm{d}z = 0 \quad \text{for} \quad m \leq M. \tag{17}$$

By definition wavelets act as multiscale M^{th} order differential operators (Herrmann, 1997; Mallat, 1997). This property explains why wavelets trigger on the singular behavior in the data's M^{th}-order derivative. By examining the wavelet coefficients as a function of the wavelet's scale, σ, possible singular behavior in f can be detected and measured.

Wavelet theory (Jaffard, 1991; Mallat and Hwang, 1992; Bacry *et al.*, 1993; Holschneider, 1995; Jaffard and Meyer, 1996; Herrmann, 1997, 1998b; Dessing, 1997) makes statements on the singular behavior precise by providing detailed estimates for the decay rate of the wavelet coefficients along lines where the wavelet coefficients modulus has local

maxima, i.e. where $\partial_z \mathcal{W}\{f,\psi\}(\sigma_1, z=0)$. These lines connect the moduli maxima and are called wavelet transform modulus maxima lines, WTMML's. As the scale decreased they point to the location of the singularities in f while they yield, under particular conditions, the following estimate for the wavelet coefficient's decay rate (Jaffard, 1991; Mallat and Hwang, 1992; Holschneider, 1995; Mallat, 1997)

$$|\mathcal{W}\{f,\psi\}(\sigma,z)| \leq C\sigma^{\alpha} \quad \text{as} \quad \sigma \to 0. \tag{18}$$

Given this estimate, where C is a finite wavelet-dependent constant, local scaling can be measured by the scale exponent α. This scale exponent, also known as a Hölder exponent, measures the sharpness of transitions in f.

Generalized Transitions

Onset functions (Gelfand and Shilov, 1964; Zemanian, 1965; Holschneider,1995) of the type

$$\chi_{+}^{\alpha}(z) \triangleq \begin{cases} 0 & z \leq 0 \\ \frac{z^{\alpha}}{\Gamma(\alpha+1)} & z > 0, \end{cases} \tag{19}$$

$$\chi_{-}^{\alpha}(z) \triangleq \begin{cases} \frac{-z^{\alpha}}{\Gamma(\alpha+1)} & z \leq 0 \\ 0 & z > 0, \end{cases} \tag{20}$$

are used to model transitions with varying order α. Γ denotes the Gamma function while α controls the scaling and sharpness of the transitions (Herrmann, 1998a). Substitution of equations 19–20 into equation 16 yields an exact scaling behavior for the wavelet coefficients of the type presented in equation 18, i.e.

$$|\mathcal{W}\{f,\psi\}(\sigma,z)| = C'\sigma^{\alpha}, \tag{21}$$

where C' is again a finite constant[5], depending on the wavelet only. For $\alpha = 0$ the definition of equations 19-20 corresponds to a jump discontinuity. For $\alpha = 1$ the onset functions become a ramp function, while for $\alpha = -1$ the onsets become Dirac's generalized function. To summarize, α describes the sharpness, irrespective of the scale. As such the exponent quantifies the *order of magnitude* of the variations at singular onsets, which act under convolution as (anti-)causal fractional differential ($\alpha \leq -1$) or integration ($\alpha \geq -1$) operators.

Combinations of equal sharpness onset functions, as defined in equations 19 and 20, are used to define media profiles with generalized transitions. These profiles are defined as

$$f(z) = c_{+}\chi_{+}^{\alpha}(z) + c_{-}\chi_{-}^{\alpha}(z) + P_n(z), \tag{22}$$

[5]Holschneider (1995) shows that this constant is the Mellin transform of the wavelet transform, evaluated at the argument $\alpha + 1$.

where $P_n(z)$ is an n^{th}-order polynomial. By setting the number of vanishing moments to $M > n$ the wavelet transform scales as

$$|\mathcal{W}\{f,\psi\}(\sigma,z)| \leq C\sigma^{\alpha} \quad \text{as} \quad \sigma \to 0 \tag{23}$$

along the WTMML. Choosing $M > n$ is important because otherwise no local modulus maxima may be found, or the wrong scaling may be estimated,

$$|\mathcal{W}\{f,\psi\}(\sigma,z)| \leq C\sigma^{M} \quad \text{as} \quad \sigma \to 0. \tag{24}$$

The latter case arises when f is being smoothed and $\sigma \ll \sigma_s$ with σ_s the smoothing scale.

Figures 1, 2 and 3 illustrate the significance of the sharpness for the description of transitions and their induced reflectivity. In Figure 1 generalizations of the jump discontinuity are depicted together with the signatures for the corresponding normal incidence reflectivity. As the transition becomes smoother (α larger) the reflection signatures become more integrated, eventually loosing their zero crossings. Nonsymmetry issues related with transitions other than jumps are illustrated in Figure 2. Finally, the scaling of the migrated and stacked reflectivity is shown in Figure 3. The reflectivity modeling involves running an acoustic layercode on a medium with the compressional wave speed given by equation 22 with $c_+ = 1271\,\text{m/s}$, $c_- = 0$ and $P_0 = 3156\,\text{m/s}$. The density, ρ is given by the same equation but now with $c_+ = 126\,\text{kg/m}^3$ and $P_0 = 2494\,\text{kg/m}^3$. The scale exponents are taken to be the same for all medium properties and have the following three values, $\alpha \in \{-0.99\ -0.04\,0.68\}$, see Figure 3 (left). Figure 3 (middle) shows that varying the temporal frequency content of the source wavelet changes the spatial scale of the stacked seismic reflectivity. While the scaling of the middle bin is consistent with that of a delta distribution, the first and third bins display a different behavior for their maxima. Hence, this figure is a first indication that α-order transitions give rise to a frequency/scale dependent imaged and stacked reflectivity. Here, the scale is the reciprocal of the central frequency. As will be shown later, migration is a process that reconstructs the singular scaling behavior of reflectors (Symes, 1995).

Reflectivity as the Continuous Wavelet Transform

The single plane wave examples in the previous section showed the presence of a relationship between the scaling of a transition and the imaged reflectivity. While this is an interesting result its implication is limited because seismic waves essentially probe the earth at a single more or less fixed scale. However, for multiple angle AVO, the observation becomes the effective wavelength increases as a function of an increasing angle of incidence, i.e. $\lambda_z \sim \lambda_0 \cos^{-1}\bar{\theta}(\mathrm{p})$ with λ_0 the wavelength for normal incidence.

Besides the constant factor π^{-1}, the imaged reflectivity (cf. equation 14) corresponds exactly to the definition for the continuous wavelet transform with $M = 1$, i.e.

$$\langle R_{pp}\rangle(\mathrm{p},z) \approx \frac{1}{\pi}\bar{\mathrm{M}}(\mathrm{p})\mathcal{W}\{\mathbf{\Delta},s\}(\bar{\sigma}_{pp}(\mathrm{p}),z). \tag{25}$$

The above association makes the wavelet transform highly relevant for better understanding imaged seismic reflectivity. Another implication is the emergence of an additional angle dependent term, not present in the conventional formulation for AVO.

AVO ANALYSIS

Pre-stack migrated data are widely used to study the angle dependence (AVO) of imaged reflectivity. In these analyses the medium is tacitly assumed to consist of well-separated zero-order jump discontinuities. Unfortunately, this assumption is difficult to justify given multiscale analysis findings on well data (Herrmann, 1997, 1998b; Herrmann and Stark, 2000) as an example. In fact the earth can be shown to consist of an accumulation of different order transitions. The order variation and accumulation give rise to different order transitions to emerge practically everywhere, i.e. at every abscissa and length scale.

Direct implications of multifractal behavior are the existence of non-zero order transitions and the invalidity of sufficient distance separation for the discontinuities. At the seismic scale range both these properties not only give rise to a complicated scaling behavior, which can effectively be characterized by the local scale exponent α, but may also be responsible for anomalous AVO behavior. For instance, when the medium fluctuations locally scale with an $\alpha = -1$, a direct hydrocarbon indicator, based on linearized Zoeppritz (Castagna and Backus, 1993; van Wijngaarden, 1998) will erroneously detect a bright spot.

Linearized Zoeppritz Inversion

For a medium with isolated[6] jump discontinuities inversion for the normalized fluctuations is possible, given some *prior* on a slowly varying background medium. For a medium with N jump discontinuities the modeled reflectivity reads

$$R_{pp}(\mathrm{p}, z) \approx \bar{\mathrm{M}}(\mathrm{p})\bar{\sigma}_{pp}(\mathrm{p})(\boldsymbol{\Delta}' * s_\sigma)(z) \tag{26}$$

with

$$\boldsymbol{\Delta}(z) = \sum_{i=1}^{N} \begin{pmatrix} \Delta_i \mathbb{Z} \\ \Delta_i c_p \\ \Delta_i \mu \end{pmatrix} \delta(z - z_i). \tag{27}$$

Normalized fluctuations are defined as $\Delta_i f \triangleq \frac{\delta_i f}{\bar{f}_i}$ where $\delta_i f \triangleq f(z_i + \epsilon) - f(z_i - \epsilon)$ and $\bar{f} \triangleq [f(z_i + \epsilon) + f(z_i - \epsilon)]/2$ with $\epsilon \downarrow 0$. The above definition for reflection density forms the basis of the majority of AVO analyses techniques, where angle dependence of the reflection coefficients as defined in equations 26–27 is prototype. These reflection coefficients are computed from the data by deconvolution, which when successful,

[6]Isolated means that the distance between the consecutive reflectors has to be large compared to the the dominant spatial wavelength.

reveals a behavior more or less consistent with modeled reflection coefficients, i.e. the $\bar{\mathrm{M}}(\mathrm{p})\boldsymbol{\Delta}'(z)$ without the contribution of the source wavelet. What remains is to solve for the normalized fluctuations, which is relatively straightforward because the reflection coefficients are linear in the fluctuations. A slowly varying *prior* is used to defined the nonlinear part, $\bar{\mathrm{M}}(\mathrm{p})$, of the reflection coefficients.

Actual inversion is performed on each discretization point of the imaged and deconvolved reflectivity. The inversion itself is based on minimizing the mismatch between the measured and the modeled data. For a single reflector located at $z = z_i$, the forward model reads (Aki and Richard, 1980; van Wijngaarden, 1998)

$$\begin{pmatrix} R_{pp}(\mathrm{p}_1, z=z_i) \\ \vdots \\ R_{pp}(\mathrm{p}_n, z=z_i) \end{pmatrix} = \begin{pmatrix} \frac{1}{2} & \frac{1}{2}\frac{\bar{c}_p^2\mathrm{p}_1^2}{\cos\theta_p(\mathrm{p}_1)} & -2\bar{c}_s^2\mathrm{p}_1^2 \\ \vdots & \vdots & \vdots \\ \frac{1}{2} & \frac{1}{2}\frac{\bar{c}_p^2\mathrm{p}_n^2}{\cos\theta_p(\mathrm{p}_n)} & -2\bar{c}_s^2\mathrm{p}_n^2 \end{pmatrix} \begin{pmatrix} \Delta_i\mathbb{Z} \\ \Delta_i c_p \\ \Delta_i\mu \end{pmatrix} + \begin{pmatrix} n_1 \\ \vdots \\ n_n \end{pmatrix}$$

$$\mathbf{d}_f = \mathbf{A}_f\boldsymbol{\lambda} + \mathbf{n}, \tag{28}$$

where the amplitude *versus* p (AVP) behavior is discretized over $\mathrm{p} = \mathrm{p}_1 \cdots \mathrm{p}_n$. The $\mathbf{d}_f$ is a vector with the forward modeled data, and $\mathbf{n}$ is a residue vector that contains the remaining nonlinear behavior. By minimizing, for each fixed depth level $z = z_i$, the modeled *versus* measured AVP behavior, i.e. minimizing $\|\mathbf{d}_m - \mathbf{A}_f\boldsymbol{\lambda}\|^2$ as a function of $\boldsymbol{\lambda}$ with $k = 1 \cdots n$, the vector with the normalized fluctuations is estimated.

Singular value decomposition (Menke, 1984; van Wijngaarden, 1998) is used to carry out the inversion, which involves a decomposition of the $3 \times n$ forward model matrix, $\mathbf{A}_f$, into

$$\mathbf{A}_f = \mathbf{U}\mathbf{S}\mathbf{V}^T, \tag{29}$$

with $\mathbf{U}$ an $n \times n$ matrix with vectors that span the model data space, $\mathbf{S}$ a diagonal $n \times 3$ matrix with singular values, and $\mathbf{V}^T$ a 3×3 matrix spanning the model space. The generalized inversion, which solves for the fluctuations vector, reads

$$\boldsymbol{\lambda} = \mathbf{V}[\mathbf{S}^T\mathbf{S}]^{-1}\mathbf{S}^T\mathbf{U}^\mathbf{T}\mathbf{d}, \tag{30}$$

with the corresponding forward modeled data given by

$$\boldsymbol{\lambda}_f = \mathbf{A}_f\boldsymbol{\lambda}. \tag{31}$$

Figures 4 and 5 summarize the linearized Zoeppritz inversion results for an acoustic medium, defined by two homogeneous halfspaces with the upper halfspace given by $c_p = 3156\,\mathrm{m/s}$, $\rho = 2494\,\mathrm{kg/m^3}$, and the lower halfspace given by $c_p = 4427\,\mathrm{m/s}$, $\rho = 2620, \mathrm{kg/m^3}$. The elastic equations simplify to their acoustic counterparts by setting the shear wavespeeds, c_s, to zero.

The procedure applied to a synthetic shot record (see Figure 4 top) comprises the following steps

1. A depth migration, based on equations 3 and 4, yielding an imaged $(\tau - \mathrm{p})$-domain reflectivity gather (see Figure 4 bottom). Input to the migration are shot records of the type depicted in Figure 4(top). The velocity of the upper halfspace is used for the migration.

2. Picking of the local maxima, yielding the AVP behavior (see Figures 4 and 5).

3. Linearized Zoeppritz inversion based on equations 28–31. The medium properties of the upper halfspace are used as *priors* in the inversion (see Figure 5 on the right for the inverted profiles).

We used an elastic layercode program to generate the shot record, with the slowness set to a range corresponding to an angle of incidence of $\theta_p(\mathrm{p}) \in [0,\ 80]$ degrees. We used only local maxima of the imaged gather to reduce computational costs. Comparison of the inverted fluctuations (cf. equations 28-31) and the actual ones shows that the fluctuations have been estimated accurately. The observed difference is due to the fact that the original medium has a transition slightly sharper then a jump.

What Goes Wrong and Why?

The example in the previous section (cf. Figure 5) shows that the normalized fluctuations can be inverted from the AVP behavior of the imaged reflectivity. As the angles in the reflectivity gather increase, one observes a broadening of the reconstructed wavefield in the reflectivity gather (see Figure 5). The broadening is consistent with equation 25, which predicts the seismic observation scale to increase with the angle of incidence. For zero order medium transitions, this broadening does not have an effect on AVP behavior because the jump discontinuity yields reflection amplitudes that do not vary with the scale, despite an obvious increase in the observation scale, $\bar{\sigma}_{pp}(\mathrm{p}) \sim \cos^{-1}\bar{\theta}_p(\mathrm{p})$.

What if the transitions in the medium are not limited to jumps only? And what if not every discretization point corresponds to a layer transitions, as assumed in standard Zoeppritz inversion? To answer these questions, we conduct a second experiment where the order of the transition is set to $\alpha = -0.9859$, while keeping all other settings the same. The results of this experiment are summarized in Figures 6 and 7. Already from the forward modeled shot record one can see that the amplitude *versus* offset behavior is affected by the deviating transition. The AVP behavior is now given by the local maxima of

$$\langle R_{pp}\rangle(\mathrm{p}, z) \approx \frac{1}{\pi} \overbrace{\bar{\mathrm{M}}(\mathrm{p})}^{\text{intrinsic AVP}} \underbrace{\mathcal{W}\{\Delta, s\}(\bar{\sigma}_{pp}(\mathrm{p}), z)}_{\text{scaling AVP}} \tag{32}$$

which are, along the WTMML, expected to scale as

$$\langle R_{pp}\rangle(\mathrm{p}, z) \propto \bar{\mathrm{M}}(\mathrm{p})\bar{\sigma}^{\alpha}_{pp}(\mathrm{p}) \propto \bar{\mathrm{M}}(\mathrm{p})\cos^{-\alpha}\bar{\theta}_p(\mathrm{p}) \quad \text{as} \quad \mathrm{p} \to 0. \tag{33}$$

The $\propto$-sign was used to indicate that the above identities hold *modulo* some finite wavelet dependent constant.

For a transition with $\alpha = 0$ the scaling term remains constant and the reflectivity is fully determined by the intrinsic AVO contribution (see Figures 4 and 5). However, for pathological cases where $\alpha \neq 0$ a deviating behavior will be observed, possibly yielding inaccurate results for the Zoeppritz inversion. The example depicted in Figures 6 and 7 confirms this inaccuracy and clearly shows that the Zoeppritz inversion not only fails to estimate the correct magnitudes for the variations, but also fails to reconstruct the sharpness of the transition. Clearly, this type of behavior is related to the fact that equations 26–28 are based on transitions of zero order ($\alpha = 0$).

Situations where $\alpha \neq 0$ are not limited to medium variations that are defined by equation 22, but occur whenever the wavelet coefficients of the medium fluctuations become scale-dependent. For instance, across the seismic scale range, actual well-log measurements display a highly heterogeneous scaling behavior with local scale exponents that range over $\alpha_{\text{observe}} \in [-1, 3]$. These wild fluctuations are not limited to the WTMML but apply to all sample points. As a consequence, the scaling can give rise to misinterpretations of the observed AVO behavior. For instance, in the case the velocity profile has a fine scale bump, given by a box-car or Gaussian bell-shape function, Zoeppritz inversion may identify a bright spot, yielding an inverted velocity much lower than the actual one. In this particular case the bump acts as an approximation to the delta distribution ($\alpha = -1$) which behaves as

$$\langle R_{pp}(\mathrm{p}, z) \rangle \propto \cos^{-1} \bar{\theta}_p(\mathrm{p}) \tag{34}$$

instead of the expected

$$R_{pp}(\mathrm{p}, z) \approx 2 \cos^{-2} \bar{\theta}_p(\mathrm{p}) \Delta_i c_p. \tag{35}$$

for a jump in the velocity.

SCALE RENORMALIZATION BY MONOSCALE ANALYSIS

Monoscale analysis provides information on the order of the transitions (Herrmann and Stark, 1999, 2000; Stark and Herrmann, 2000). This information can be used to "correct" for the observed AVP behavior by invoking a scale re-normalization based on the monoscale findings. Correcting for apparent "fine-layering" AVP is not new. For example, Wapenaar *et al.* (1999) recently proposed to project the largest effective wavelength, the wavelength that pertains to the largest angle of incidence, on to the imaged reflectivity. In this way they are able to keep the seismic observation scale angle independent and fixed. The remaining AVP behavior is, after this additional bandwidth limitation, indicative for the intrinsic AVP. For an isolated transition this method works fine and has the advantage that no information on the order of the transition is required. However, for complicated media, such as given by well-log data, the additional filtering has the disadvantage that it goes at the expense of an unwanted decrease in resolution.

Instead, the method we present in this paper proposes a renormalization of the observed imaged reflectivity. In order to apply the proper renormalization information on the order of the transition, underlying the reflectivity is required. As shown by Herrmann and Stark (1999, 2000) and Stark and Herrmann (2000), this type of information can be obtained from inherently bandwidth limited data, using the monoscale analysis method. Next, we describe briefly the main principle behind this method, followed by the introduction of a scheme for renormalization.

Monoscale Analysis

Traditionally, multiscale wavelet transforms are used to characterize the order of transitions/edges (Herrmann, 19981; Herrmann and Stark, 1999). Unfortunately, these multiscale methods are not applicable in cases where either the scale/bandwidth content of the data is too limited or where the data contains too many interfering transitions. Unfortunately, both situations are typical for seismic data, withstanding a truly successful and unambiguous estimation of the scale exponents.

By extending the wavelet transform to a transform with the scale fixed and wavelet order varied (Herrmann and Stark, 2000; Stark and Herrmann, 2000), i.e.,

$$\mathcal{W}_\beta\{f,\phi\}(\sigma,z) \quad \triangleq \quad \sigma^\beta \frac{\mathrm{d}^\beta}{\mathrm{d}z^\beta}(f * \phi_\sigma)(z), \tag{36}$$

one is able to analyze different types of transitions from both broadband well and single band seismic data. The convolution with ϕ, a Gaussian bell shape function with a width proportional to the scale σ, smoothes the data to the fixed scale, while the β controls the amount of sharpening $\beta > 0$ or desharpening $\beta < 0$. By varying this β fractionally, one is able to detect and estimate the order of the transitions via the following two on-off criteria (Herrmann and Stark, 1999, 2000; Stark and Herrmann, 2000);

- For transitions with $\alpha \geq 0$ and $\beta \in \mathbb{R}^+$,

$$\alpha(\sigma,x) = \inf_\beta\{\partial_x \mathcal{W}_\beta\{f,\phi\}(\sigma,x) = 0\}. \tag{37}$$

- For reflection events with $\alpha < 0$ and $\beta \in \mathbb{R}_0^-$,

$$\alpha(\sigma,x) = \sup_\beta\{\partial_x \mathcal{W}_\beta\{f,\phi\}(\sigma,x) = 0\}. \tag{38}$$

These criteria represent the property that for a positive order onset function ($\alpha \geq 0$) a local modulus maxima emerges when the order of fractional differentiation ($\beta > 0$) in Eq. 36 infinitesimally exceeds the order of the transition α. Conversely, for a differentiated transition, i.e., a reflection event with $\alpha < 0$, the local modulus maxima disappear when the order of fractional integration ($\beta \leq 0$) infinitesimally exceeds the negative order α.

As shown in Figure 2 the onset functions can be right-or left-handed and flipped in sign. The onset-criteria, as depicted in Eq. 37 and 38, are affected by this directivity. To circumvent this problem the β-transform (Eq. 36–38) is conducted using causal and anti-causal derivatives or integrals. In Figure 8, an example is given on the directional analysis of a synthetic example which contains smoothed causal and anti-causal onset functions as depicted on the top. The location and direction of the singularities are color coded in the third plot from the top.

Renormalization

Given information on the order of the transitions responsible for the reflection, one is able to correct for the scaling contribution observed in the apparent AVP behavior. This scaling contribution gives rise to deviatingAVP behavior which directly affects the Zoeppritz inversion. However, after renormalization the intrinsic AVP behavior is expected to be restored, yielding more accurate estimates for the fluctuations from the Zoeppritz inversion.

The proposed inversion process consists of the following steps:

1. Apply a depth migration along the lines of equations 3 and 4, yielding a measured $(\tau - \mathrm{p})$-domain reflectivity gather.

2. Conduct a monoscale analysis on either the post-stack migrated data or on the imaged reflectivity gather itself, yielding for every reflector a single α_i estimate or multiple α estimates for each slowness, $\alpha_i(\mathrm{p}_k)$ for $k = 1 \cdots n$.

3. Obtain the AVP amplitudes by following the local extrema of the reflectivity gather.

4. Correct for each reflector the scaling contribution by

$$\mathbf{A}_f \mapsto \mathbf{\Gamma}\mathbf{A}_f \quad \text{with} \quad \mathbf{\Gamma} = \begin{pmatrix} [\cos\bar{\theta}_p(\mathrm{p}_i)]^{\alpha(\mathrm{p}_1)} & & \\ & \ddots & \\ & & [\cos\bar{\theta}_p(\mathrm{p}_n)]^{\alpha(\mathrm{p}_n)} \end{pmatrix}. \tag{39}$$

5. Conduct the Zoeppritz inversion with the corrected forward model matrix.

Smoothly varying models (the barred quantities) suffice for both the migration velocity model and the Zoeppritz inversion *prior*. In the idealistic case where the medium consists of a true[7] transition of the type defined in equation 22, monoscale analysis on the stacked or common p gathers suffices. The reason that the monoscale analysis also works on the stacked data lies in the fact that stacking corresponds to taking the inverse

[7]True algebraic singularities do not exist. However, a true algebraic singularity is referred to as a discrete function which displays a behavior as defined in equations 19 or 20 over a wide enough scale range permitted by the inner (sample interval) and outer (profile length) scales.

of the continuous wavelet transform. A function f can be reconstructed from its wavelet coefficients by means of computing the integral

$$f(z) = \mathcal{W}^{-1}\{\mathcal{W}\{f,\psi\}\}(z) \triangleq \frac{1}{c}\int_0^{+\infty} \mathcal{W}\{f,\psi\}(\sigma,z)\frac{\mathrm{d}\sigma}{\sigma}, \tag{40}$$

where c is a finite constant depending on the wavelet. The reconstruction holds *modulo* smooth polynomials when f is a tempered distribution, $f \in S'(\mathbb{R})$, e.g. delta distribution or a distribution of the type defined in equations 19 and 20 (Jaffard, 1997). Associating this expression with a renormalized stacking of the imaged reflectivity yields

$$\int_{\mathrm{p}_0}^{\mathrm{p}_1} \langle R_{pp}(\mathrm{p},z)\rangle \mathrm{dp} \quad \Longleftrightarrow \int_{\mathrm{p}_0}^{\mathrm{p}_1} \bar{\mathrm{M}}(\mathrm{p})\mathcal{W}\{\mathbf{\Delta},s\}(\bar{\sigma}_{pp}(\mathrm{p}),z)\frac{\mathrm{d}\bar{\sigma}_{pp}(\mathrm{p})}{\bar{\sigma}_{pp}(\mathrm{p})}, \tag{41}$$

where p_0 and p_1 refer to the minimum and maximum p-values, respectively. Under the assumption that the p-dependence of the $\bar{\mathrm{M}}(\mathrm{p})$ does not affect the inverse transform too much, the singular part of an ideal transition will be reconstructed during the stacking process. However, due to aperture limitation in the seismic acquisition the p-range is finite, making the reconstruction inherently bandwidth limited. Besides resolution enhancement the inverse transform of equation 42 also reduces uncorrelated noise.

When the pre-stack migrated data is of good enough quality the monoscale analysis may be conducted on common p-gathers instead. In cases where the scaling of the reflector is no longer ideal, monoscale analysis on all traces of the imaged reflectivity gather provides α estimates for each p. Equation 39 allows for a direct application of the p-dependent α estimates in the renormalization.

Before discussing examples and applications of the proposed renormalization we point out an additional problem. This problem is related to the fact that as soon as a transition is no longer a jump discontinuity the observed fluctuation depends on the scale of observation. This is why the proposed renormalization only holds within a wavelet-dependent but scale-independent constant. The constant itself is proportional to a reference scale which can be obtained when information on the wavelet is available. Absence of this information does not affect the proposed method too seriously because information on many of the lithological and direct hydrocarbon indicators depends only on the relative magnitude of the normalized fluctuations. These ratios will not be affected by the constant. Consequently, direct hydro-carbon indicators, based on these ratios, will not be affected.

Figures 9 and 10 contain a first example of the application of the proposed renormalization to a medium containing a single generalized transition of the type as defined in equation 22. The problem with the wavelet-dependent constant is temporarily solved by normalizing measured AVO-curves by the theoretical normal incidence reflection amplitude. Clearly, both the estimated AVP behavior and the corresponding linearized Zoeppritz inversion results are closer to the expected behavior, compared to the results without the renormalization, only the sharpness of the transition is not reconstructed.

RECONSTRUCTION

Given the location, sharpness and magnitude of transitions one is able to reconstruct the different medium profiles, including the specifics of the various transitions. Both the sharpness and magnitude are obtained by the monoscale analysis and renormalized Zoeppritz inversion methods as described in the previous section. The transitions are reconstructed via

$$f(z) = \int \sum_{i=1}^{N} c_{\pm}^{i} \chi_{\pm}^{\alpha_i - 1}(z - z_i) \mathrm{d}x, \tag{42}$$

where the $\chi_{\pm}^{\alpha_i - 1}$'s are the right-handed (+) or left-handed (−) transitions, defined in equations 19-20. The α_i's and z_i's are the estimated exponents and location of the singularities.

Most information in seismic data on the transitions is contained in the location and order of the singularities. Information on the regular, read differentiable, part of the transitions is lost, i.e. the normalized fluctuations and seismic reflectivity do not contain large scale fluctuations. The bottom plot of Figure 8 contains the reconstruction of the synthetic example depicted on the top. Estimates for the location, order, direction and relative magnitude are taken from both the second and third plot. The smoothing of the original function is removed by setting the smoothing of the reconstruction to zero. Because of the lacking trend there are some deviations in the reconstruction while the absolute amplitudes are also not recovered. On the other hand, the amplitude variations are nicely recovered. The deviations, e.g. between the first and second transition, are mainly do due a lack of information on the smoothing and extent of the transitions.

EXAMPLES

In this section, we review synthetic experiments. The example concerns $1\frac{1}{2}$-D medium where the seismic method and renormalization are put to the test on a medium with a single interface, whose depth and order vary laterally.

Single Interface Model

Figure 11 contains a medium with a single interface whose vertical position and order vary with off-set. The transition is normalized to yield the same increase in value across the transition for the compressional wavespeed and density. The order of the transition varies roughly between the behavior of a smooth first-order discontinuity to that of a delta function, $\alpha \in [-1, 1]$. For each lateral position $(\tau - \mathrm{p})$-domain shot records are generated, using an acoustic layercode program. The vertical number of samples and a sample interval are set to 1000 and 3 m, while the lateral number of samples was taken to be 100 with a sample interval of 60 m. Under the assumption that the reflector

can be regarded locally as horizontal, the modeled responses can be seen as the Radon transform of actually recorded seismic data.

The data are migrated using the actual[8] acoustic velocity model. The stacked migrated image is depicted in Figure 12. Three examples of migrated pre-stack reflectivity gathers at traces for which $\alpha \in \{-0.99 \; -0.04 \, 0.68\}$ are depicted in Figure 12 as well. From the reflectivity gathers, one can clearly see the difference in the pulse shape for the three gathers. These differences are an indication of the nonzeroness of the transition, an observation supported by the observed AVP, which does not correspond to that of a medium with a jump discontinuity.

Despite normalization toward the theoretical normal incidence reflection amplitude, the Zoeppritz inversions are flawed, as can be seen from Figure 13. As expected the inversion for the velocities are affected the most for the sharp interfaces, an effect predicted by equations 34 and 35. Without the normalization all estimates would have been drastically off for transitions with $\alpha \neq 0$. By invoking the proposed renormalization the Zoeppritz inversion for the velocity is significantly improved, as shown in Figure 14. The renormalization uses sharpness estimates of the reflectors obtained from the seismic data by the monoscale analysis method. For now the order of the transitions was assumed to be known.

What remains is to use the sharpness information to correctly reconstruct the transitions using equation 42. Results of this reconstruction are summarized in Figure 15, which shows a nearly perfect reconstruction for almost all the transitions. Not only the proper balance between the different fluctuations is restored but, as Figure 15 demonstrates, the sharpness is recovered as well.

CONCLUSIONS

In this paper, a simple but useful method has been introduced which corrects Zoeppritz AVO inversion for the effects induced by scaling. These scaling effects arise when at the seismic scale the reflector does not behave as a single jump discontinuity. Examples are tuning effects or differences in the characteristics of lithological boundaries.

Information on scaling is obtained using a monoscale analysis technique which provides sharpness estimates of the transitions at the seismic scale. These sharpness estimates involve the computation of scale exponents which represent order of magnitude estimates for the behavior of the wavelet coefficients.

By formulating the prestack migration in terms of the continuous wavelet transform, a possibility is created to not only reconstruct the sharpness of the reflectors but also to correct for possible anomalous AVO, induced by the scaling.

[8]Without loss of accuracy the velocity model could have been smoothed to a coarse barred velocity.

ACKNOWLEDGMENTS

This work was supported by the Borehole Acoustics and Logging/Reservoir Delineation Consortia at the Massachusetts Institute of Technology.

REFERENCES

Aki, K., and Richards, P.G., 1980, *Quantitative Seismology, Theory and Methods,* vol. 1, W. H. Freeman and Company, New York.

Bacry, E., Muzy, J. F., and Arneodo, A., 1993, Singularity spectrum of fractal signals from wavelet analysis: Exact results, —em J. Statistical Physics, 70, 635–674.

Berkhout, A. J., 1987, *Applied Seismic Wave Theory,* Elsevier, Amsterdam.

Burridge, B., and Chang, H. W., 1989, Multimode, one-dimensional wave propagation in a highly discontinuous medium, *Wave Motion, 11,* 231–249.

Castagna, J., and Backus, M., 1993, Offset-dependent reflectivity–Theory and practice of AVO analysis, Soc. of Exploration Geophysicists.

Claerbout, J. F., 1971, Toward a unified theory of reflector mapping, *Geophysics, 36,* 467–481.

de Hoop, M. V., 1992, Directional decomposition of transient acoustic wave fields, Ph.D. thesis, Delft University of Technology, Delft, the Netherlands.

de Hoop, M., 1998, Direct, leading order asymptotic, inverse scattering based on the generalized bremmer series: Direct, leading order asymptotic, inverse scattering based on the generalized bremmer series, *Mathematical and Numerical Aspects of Wave Propagation,* 249–253.

Dessing, F. J., 1997, A wavelet transform approach to seismic processing, Ph.D. thesis, Delft University of Technology, Delft, the Netherlands.

Gel'fand, I. M., and Shilov, G. E., 1964, *Generalized Functions,* vol. 1, Academic Press.

Grimbergen, J. L. T., Dessing, F. J., Wapenaar, K., and Kostek, S., 1998, Modal expansion of one-way operators in laterally varying media, *Geophysics, 63,* 995–1005.

Herrmann, F., and Stark, C., 1999, Monoscale analysis of edges/reflectors using fractional differentiations/integrations, 69rd Annual Internat. Mtg., Soc. Expl. Geophys., Expanded Abstracts.

Herrmann, F., and Stark, C., 2000, Local texture characterization of well- and seismic data by monoscale analysis, to be submitted to *GRL.*

Herrmann, F., 1997, A scaling medium representation, a discussion on well-logs, fractals and waves, Ph.D. thesis, Delft University of Technology, Delft, the Netherlands.

Herrmann, F., 1998a, Multiscale analysis of well and seismic data Multiscale analysis of well and seismic data, *Mathematical Methods in Geophysical Imaging V,* 180–208.

Herrmann, F., 1998b, Waves in multiscale media: wavelet analysis of seis- and well-data.

Holschneider, M., 1995, *Wavelets an Analysis Tool,* Oxford Science Publications.

Jaffard, S., and Meyer, Y., September 1996, *Wavelet Methods for Pointwise Regularity and Local Oscillations of Functions,* volume 123, American Mathematical Society.

Jaffard, S., 1991, Pointwise smoothness, two microlocalisation and wavelet coefficients, *Publicacions Mathematiques, 35.*

Jaffard, S., 1997, Multifractal formalism for functions part I: Results valid for all functions, *SIAM J. Mathematical Analysis, 28,* 944–970.

Jaffard, S., 1997, Multifractal formalism for functions part II: Self-similar functions, *SIAM J. Mathematical Analysis, 28,* 971–998.

Mallat, S., and Hwang, L., 1992, Singularity detection and processing with wavelets, *IEEE Transactions on Information Theory, 38,* 617–642.

Mallat, S. G., 1997, *A wavelet Tour of Signal Processing,* Academic Press.

Menke, W., 1984, *Geophysical Data Analysis: Discrete Inverse Theory,* Academic Press.

Muller, J., Bokn, I., and McCauley, J. L., 1992, Multifractal analysis of petrophysical data, *Ann. Geophysicae, 10,* 735–761.

Ostrander, W., 1994, Plane-wave reflection coefficients for gas sands at nonnormal angles of incidence, *Geophysics, 49,* 1637–1648.

Payton, C., 1997, Seismic stratigraphy—applications to hydrocarbon exploration, in *Stratigraphic Models From Seismic Data,* AAPG.

Saucier, A., and Muller, J., 1993, Use of multifractal analysis in the characterization of geological formation, —em Fractals, 1, 617–628.

Saucier, A., Huseby, O., and Muller, J., 1997, *Fractals in Engineering,* Springer.

Stark, C., and Herrmann, F., 2000, Monoscale wavelet analysis and its application to streamflow time series, to be submitted to *GRL.*

Swan, H. W., 1991, Amplitude-versus-offset measurement errors in a finely layered medium, *Geophysics, 56,* 41–49.

Swan, H. W., 1997, Removal of offset-dependent tuning in avo analysis: Removal of offset-dependent tuning in avo analysis, Society Of Exploration Geophysicists, Annual Meeting Abstracts, 175–178.

Symes, W. W., Mathematics of reflection seismology, Technical Report, The Rice Inversion Project, Rice University, 1995.

van Wijngaarden, A., 1998, Imaging and characterization of angle-dependent seismic reflection data, Ph.D. thesis, Delft University of Technology.

Wapenaar, C. P. A., and Berkhout, A. J., 1989, *Elastic Wavefield Extrapolation,* Elsevier.

Wapenaar, K., van Wijngaarden, A.-J., and van Geloven, W., 1999, Apparent AVA effects of fine-layering, *Geophysics, 64*, 1939–1948.

Wapenaar, C. P. A., 1996, One-way representation of seismic data, *Geophys. J. Internat., 178*, 178–188.

Zemanian, A. H., 1965, *Distribution Theory and Transform Analysis: An Introduction to Generalized Functions, With Applications,* McGraw-Hill, New York.

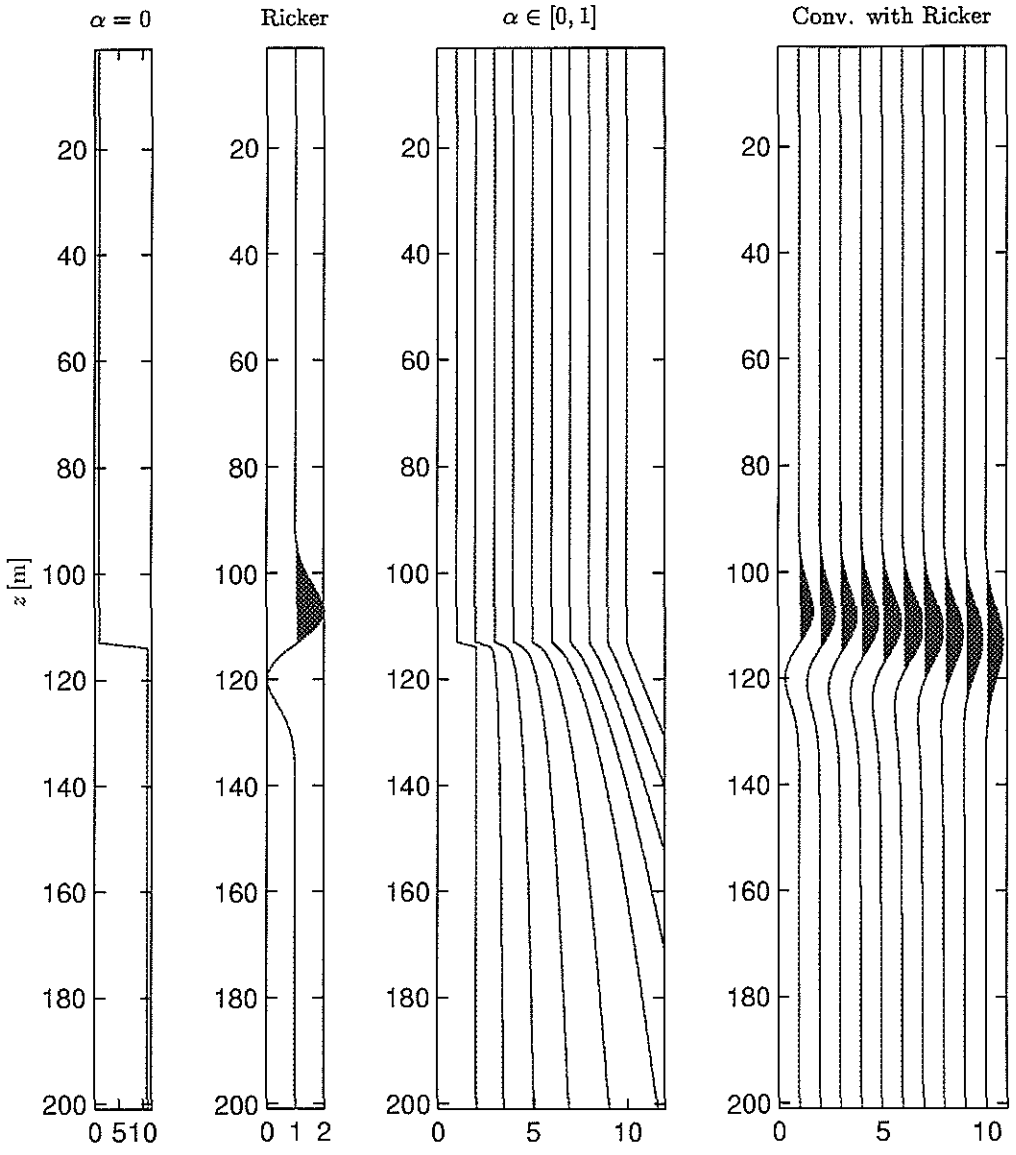

Figure 1: Generalization of edges (left) and their induced normal incidence reflectivity (right), using a Ricker wavelet and amplitude normalization. The α is the local scale exponent and ranges from 0 (left trace) to 1 (right trace). Notice the differences in the reflections (right).

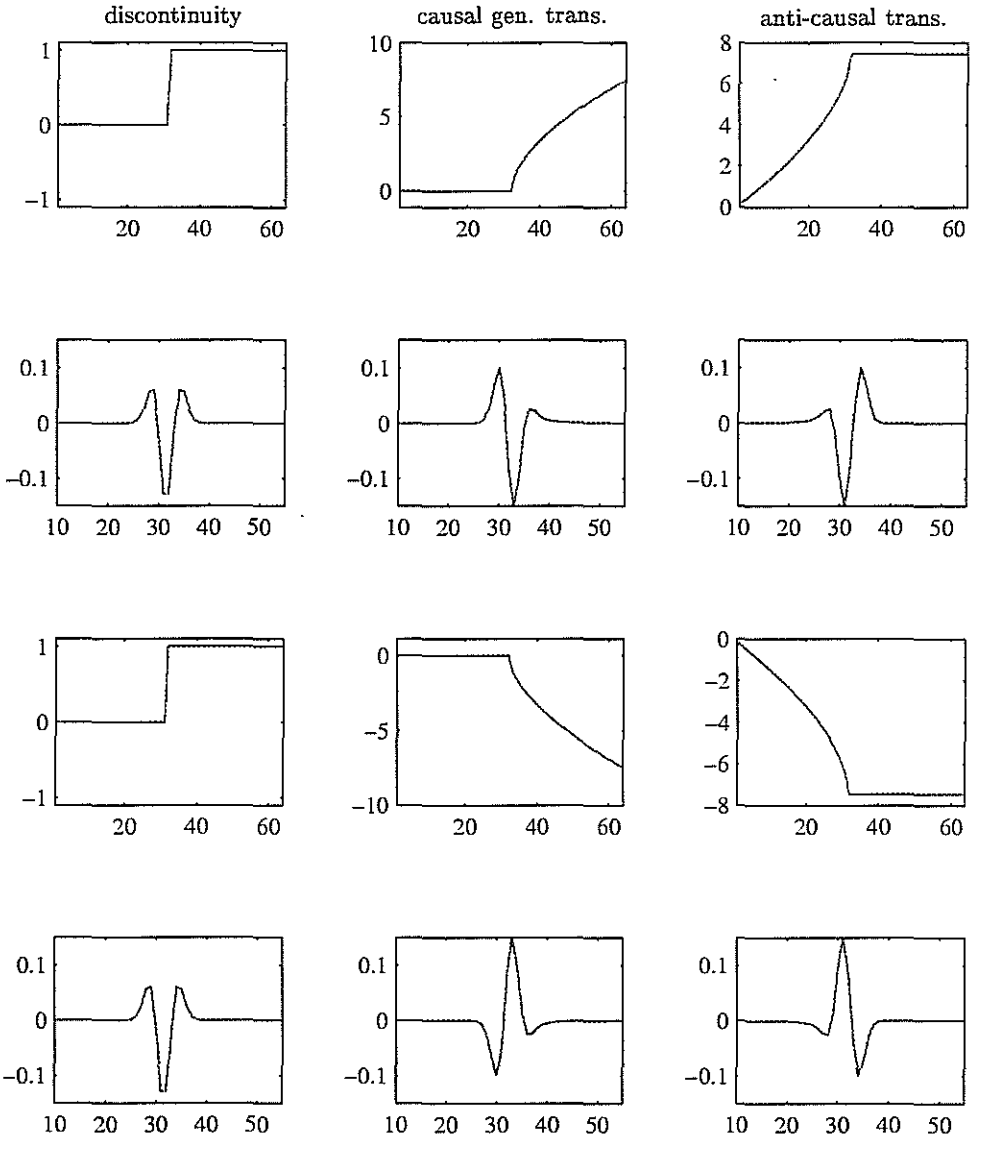

Figure 2: Examples of the generalized transitions. Notice the distinction between left and right.

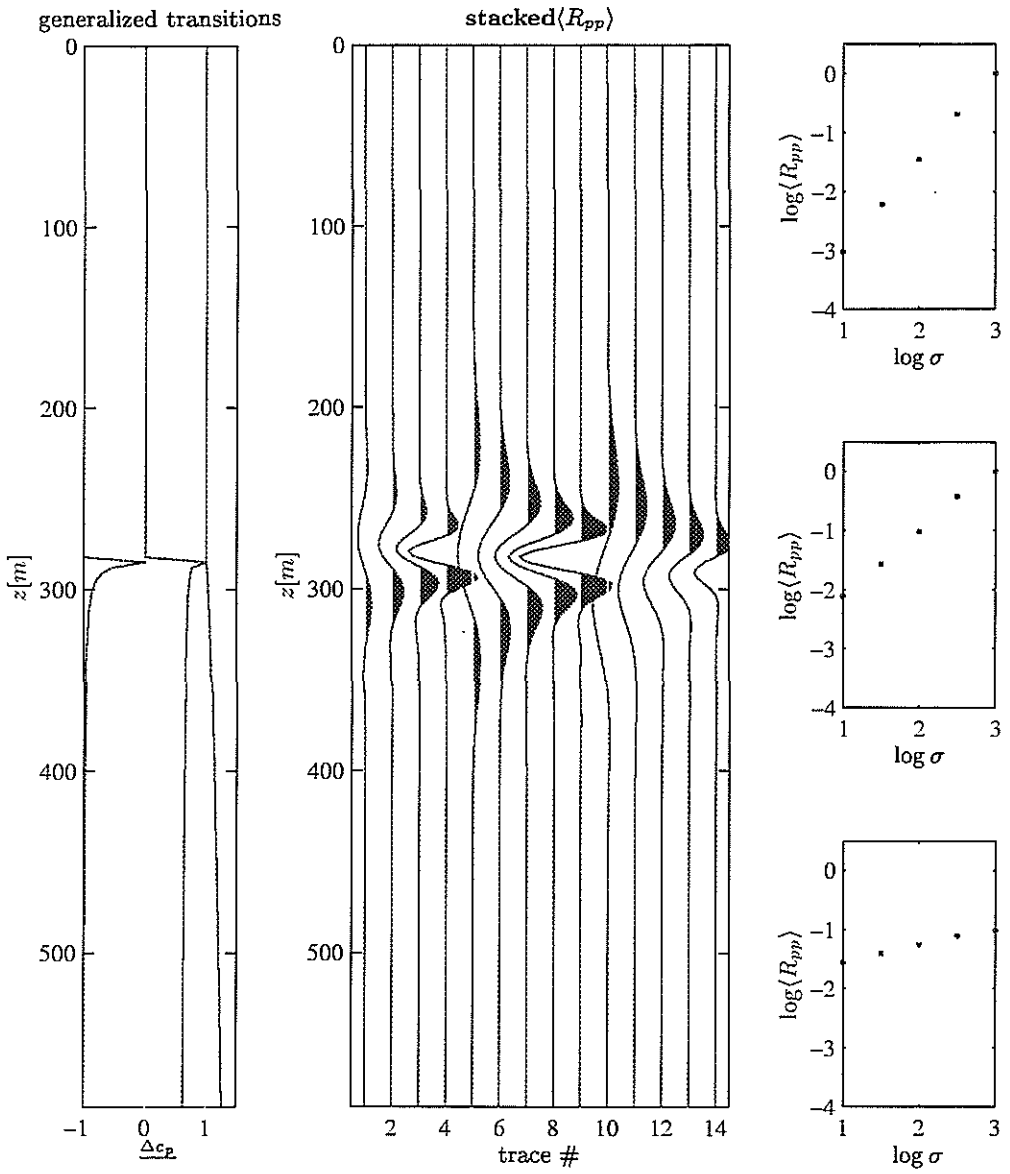

Figure 3: Scaling of α-order transitions as defined by equation 22 (left) and their induced acoustic reflectivity (middle). On the left the transition with $\alpha \in \{-0.99 \; -0.04\, 0.68\}$. Traces of the stacked migrated reflectivity are depicted in the middle for bins consisting of 5 different Ricker wavelets each. The central frequency of the Ricker wavelet is increased from left to right. On the right log-log plots for the scale (reciprocal of the central frequency) *versus* the picked maxima of the traces in the middle. Notice the significant difference in imaged reflection signatures for the different order transitions. The differences in the signatures are confirmed by the scaling of the picked maxima on the right.

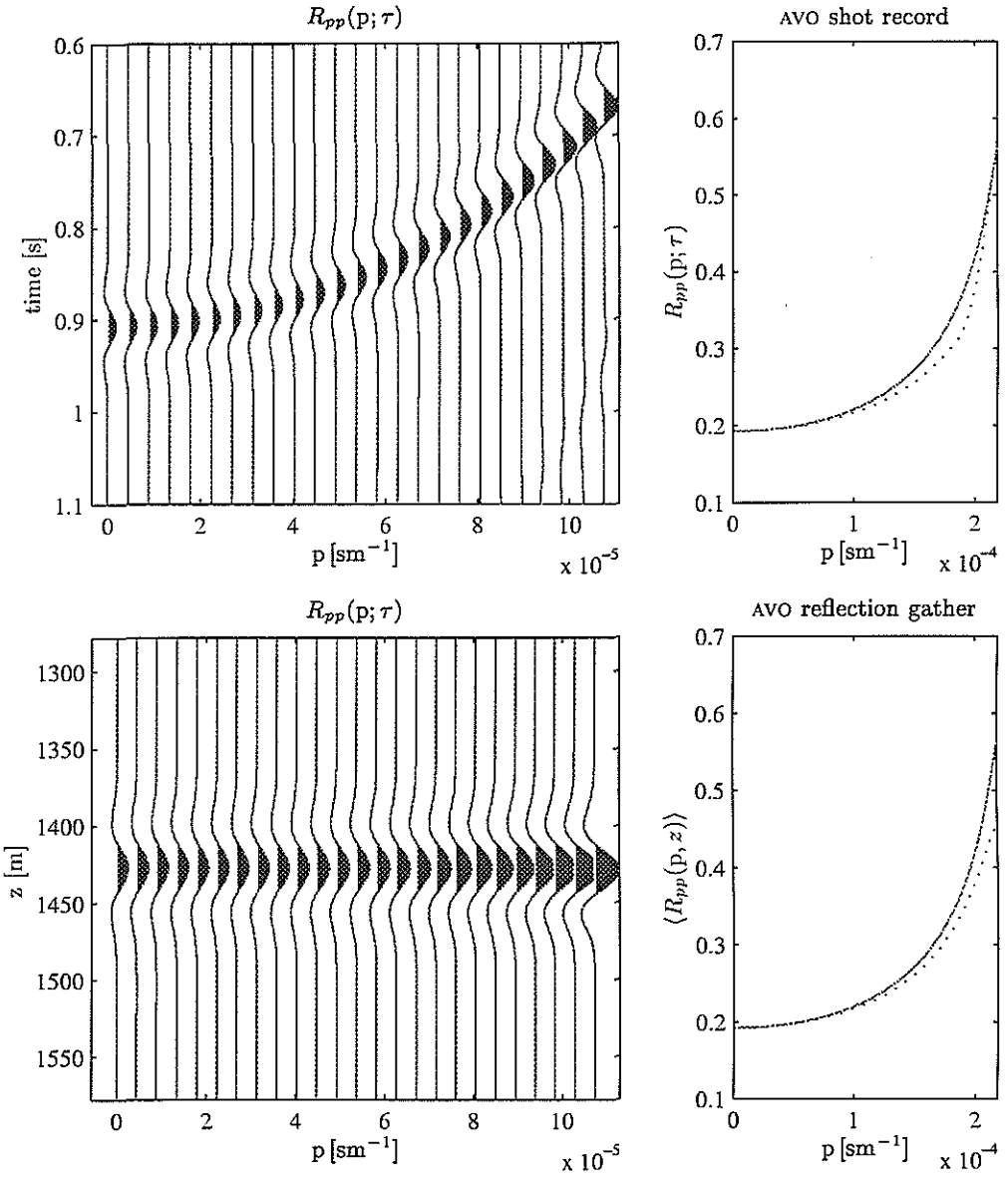

Figure 4: Modeled synthetic (τ, p)-domain shot record (top) and the corresponding imaged reflectivity (bottom). The AVO of the shot record and imaged reflectivity are plotted on the right with the dashed lines. The AVO is obtained by picking the maxima from the sections on the left and is compared with the analytic expression for the reflection coefficient (solid line), given by equations 26-27.

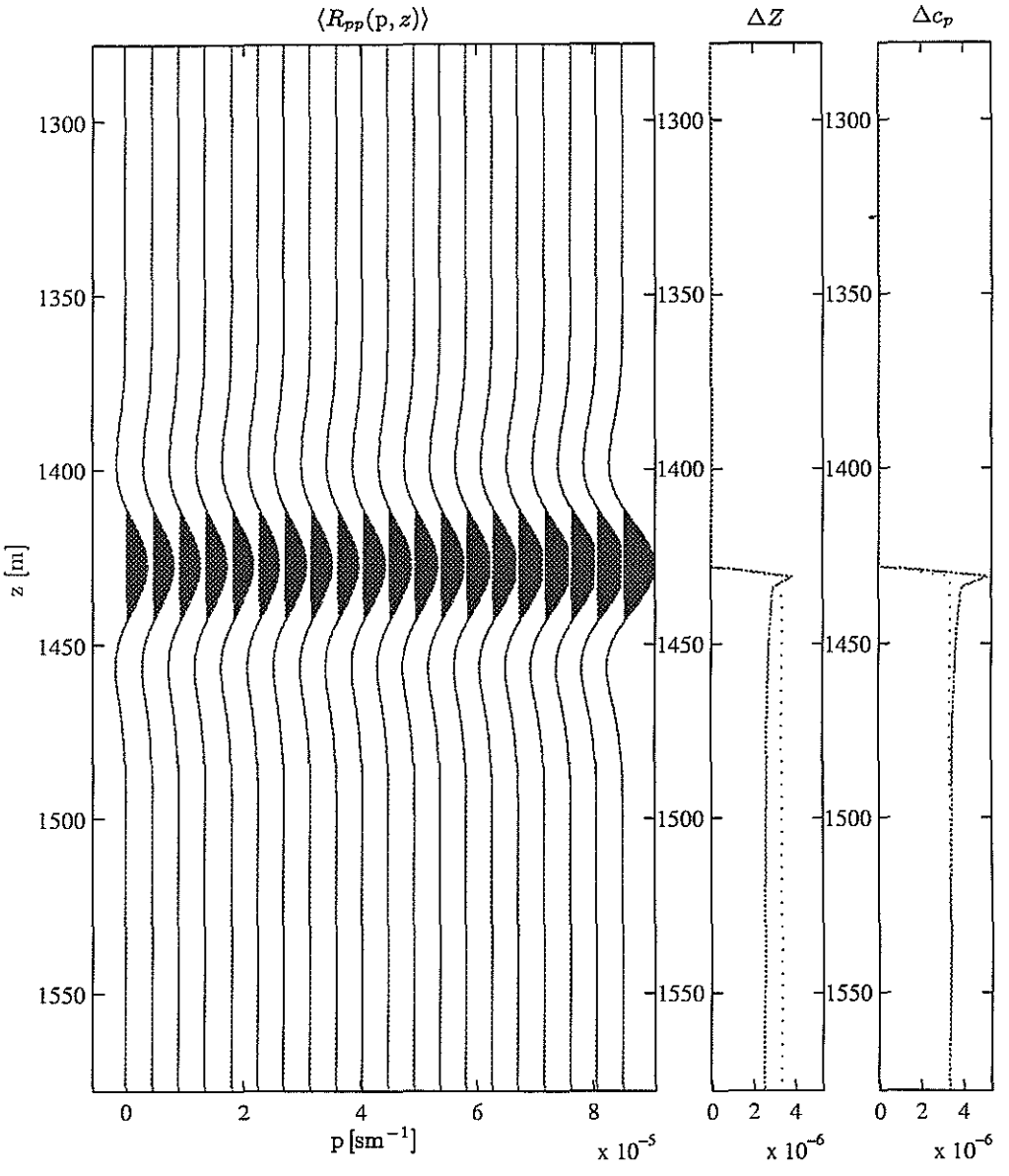

Figure 5: Imaged reflectivity gather and the Zoeppritz inverted normalized acoustic impedance (ΔZ) and compressional wavespeed (Δc_p) fluctuation profiles. Notice the good agreement between the inversion and original even though the latter (solid) was not a real jump but has a $\alpha = -0.0439$.

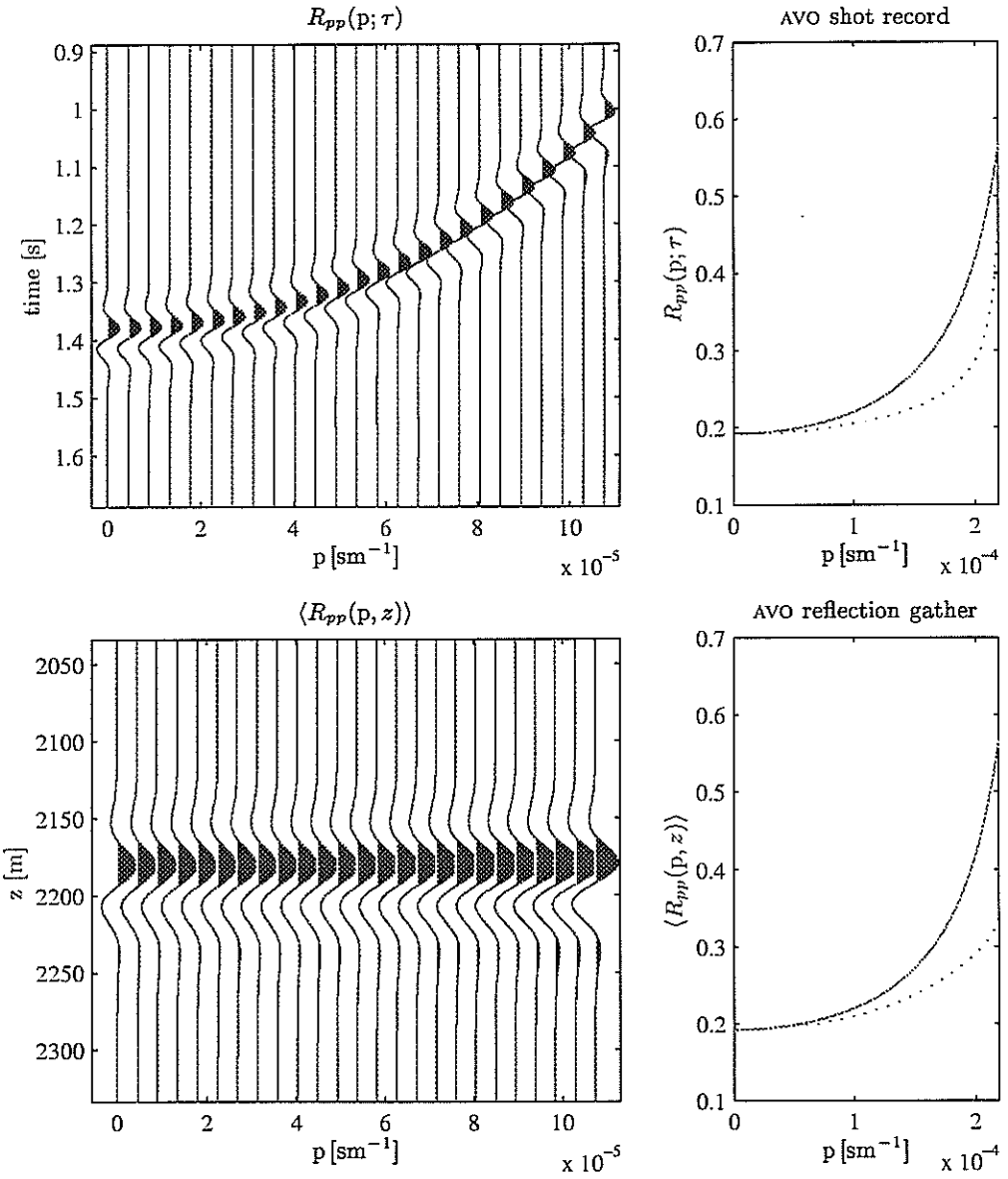

Figure 6: Same as Figure 4 but now with a α substantially differing from zero, i.e. $\alpha = -0.9859$. Besides the apparent differences in reflection signature the picked AVO behavior (dashed lines) clearly deviates from the predictions by equations 26-27 (solid lines).

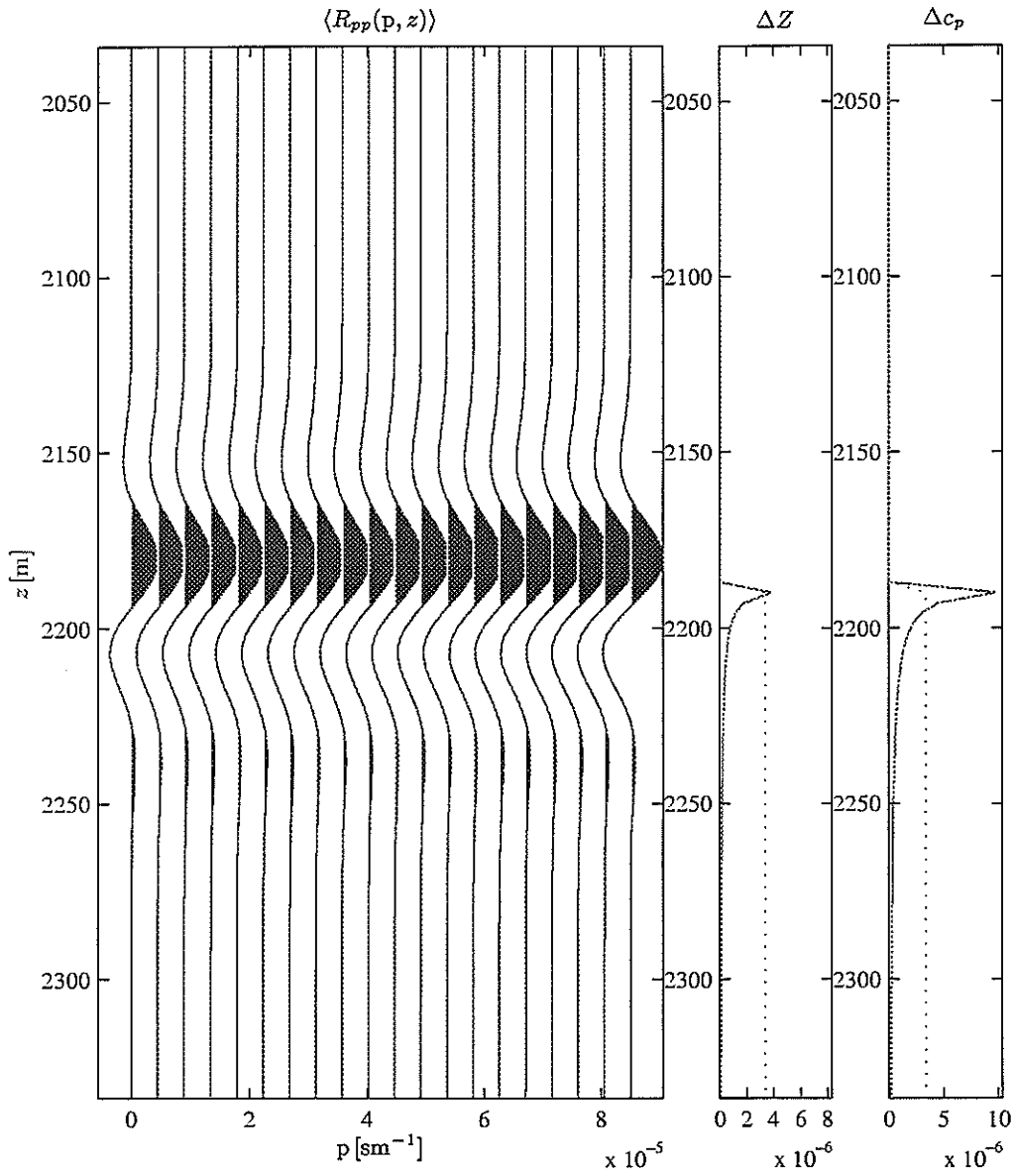

Figure 7: Same as Figure 5 but now with a α substantially differing from zero, i.e. $\alpha = -0.9859$. Zoeppritz inversion based on the picked AVO (dashed lines Figure 6) of this profile clearly does not give correct answers. In particular the inverted compressional wavespeed contrast is underestimated by more than 50% (dashed line).

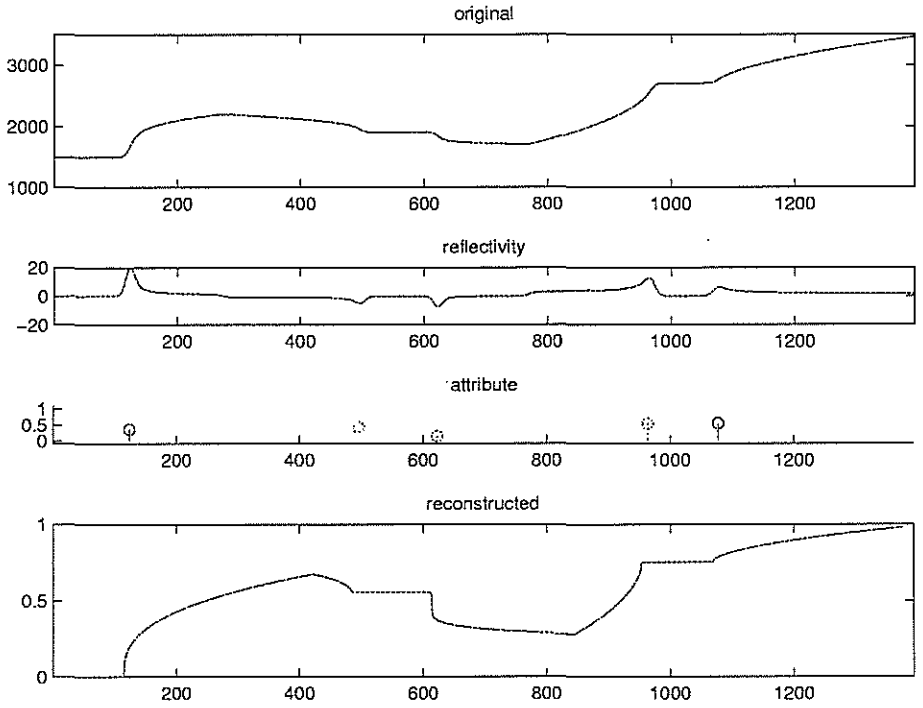

Figure 8: Example of the analysis and reconstruction of a synthetic well with different order singularities and directions. (top) the synthetic well with 5 smoothed singularities; (second plot) "reflectivity"; (third plot) position, order and direction singularities. Blue is causal positive, green anti-causal positive, red causal negative sign, magenta anti-causal negative sign. (bottom) the reconstructed profile.

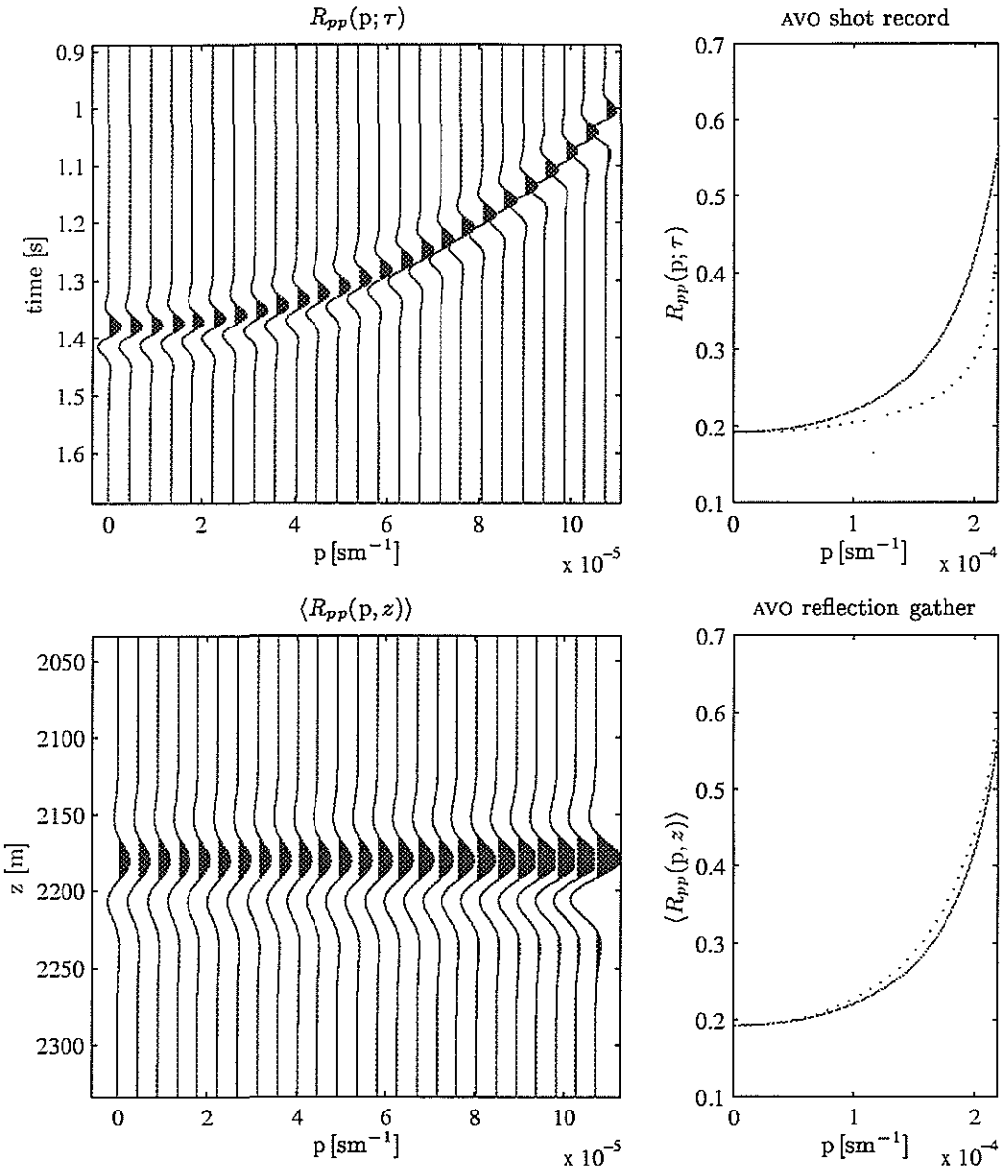

Figure 9: Same as Figure 6 but now with the correction for the picked AVO of the imaged gather (below). The correction is according equation 39 with a fixed α, obtained by the monoscale analysis. Notice the much better agreement between the theoretical (solid) and estimated (dashed) values (bottom row).

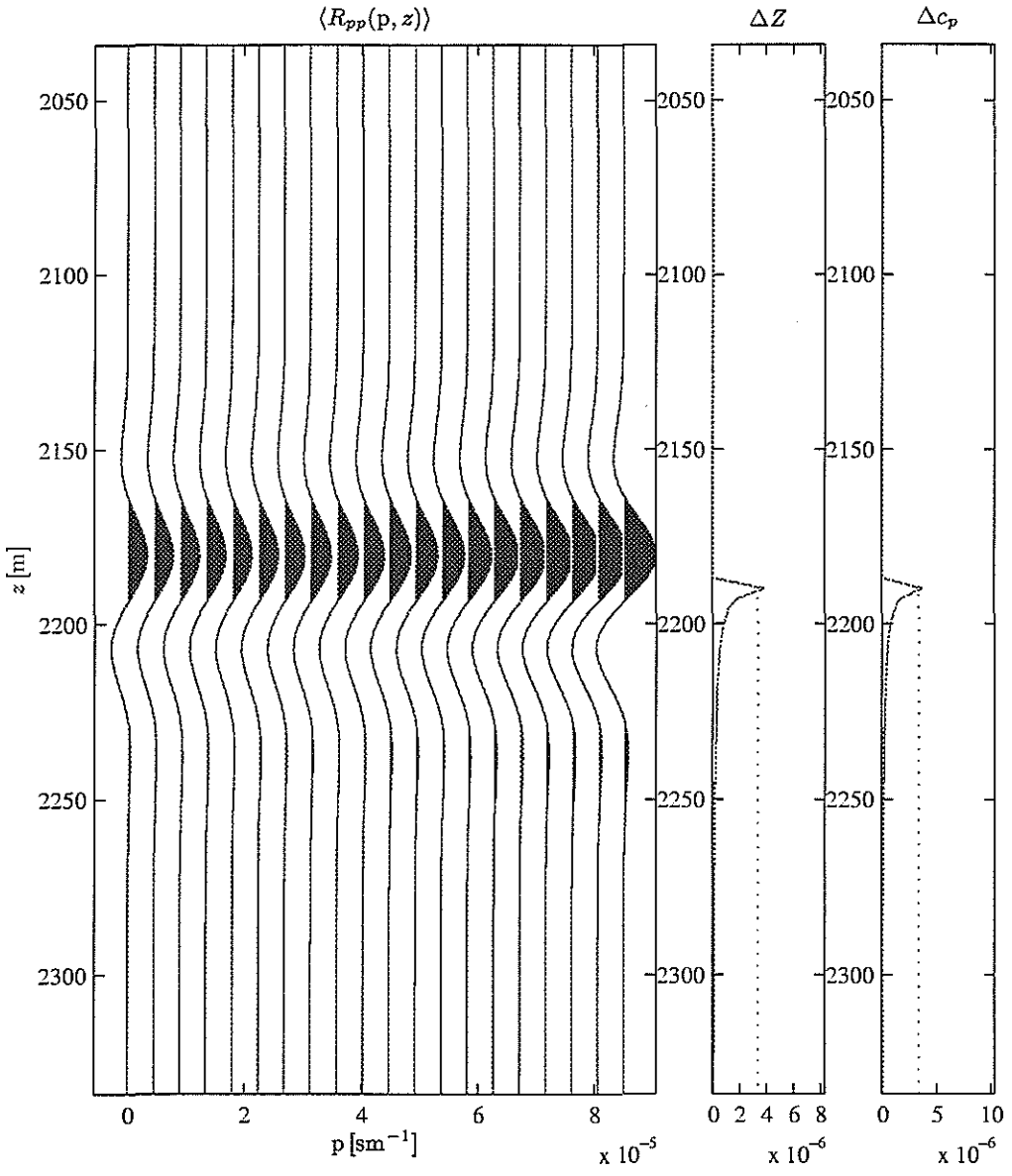

Figure 10: Corrected inversion for the AVO depicted in Figure 9. The better agreement of the AVO is also apparent in Zoeppritz inversion, which now yields satisfying estimates for the magnitude of the fluctuations (dashed lines) as compared to the original (solid lines). What remains is the correct reconstruction of the sharpness.

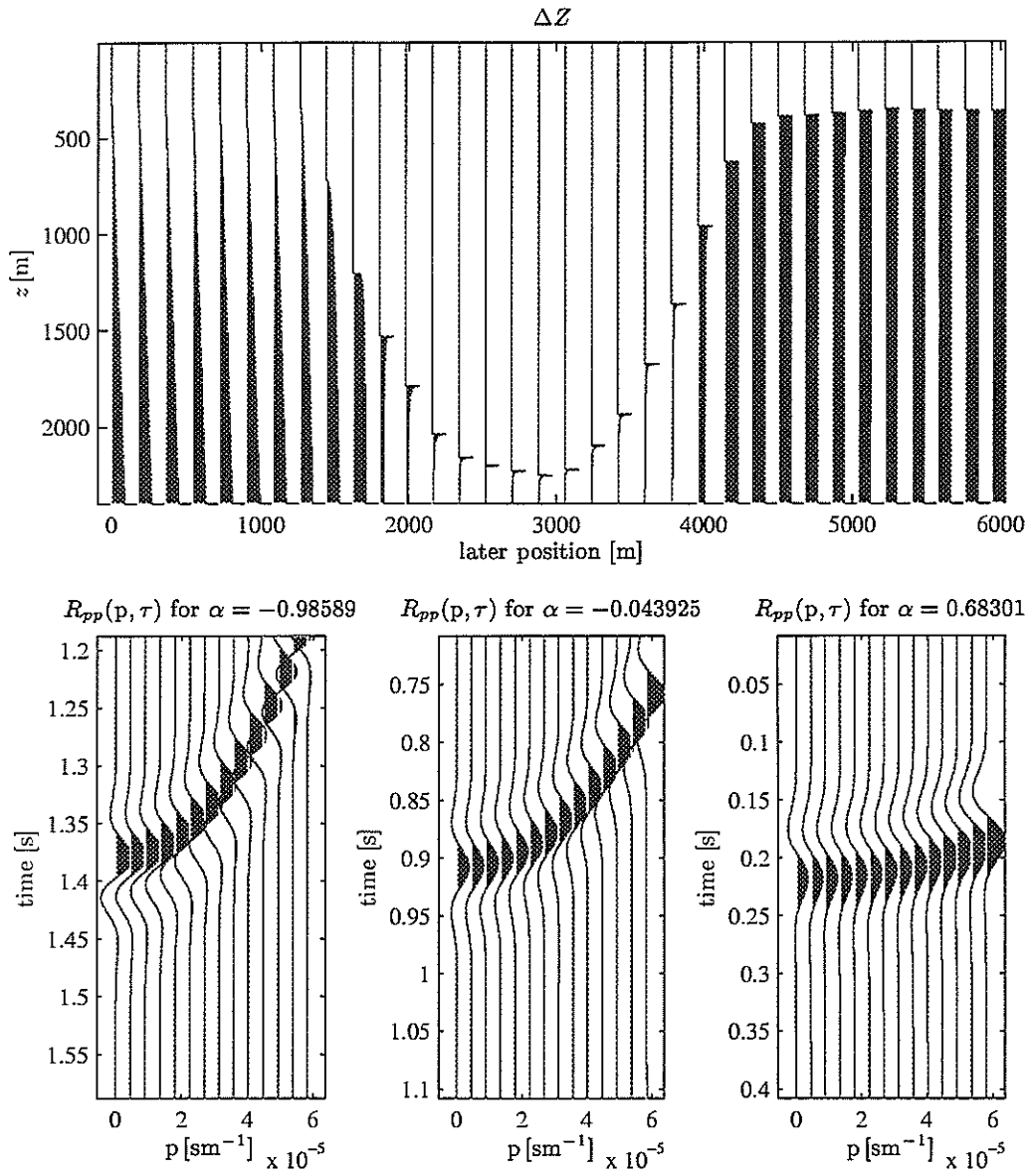

Figure 11: $1\frac{1}{2}$-D example with a medium that varies along the vertical only and that contains a single transition of varying order. On the top the fluctuations in the acoustic impedance are depicted. On the bottom one finds three shot records, obtained by running an acoustic layercode program for each lateral position while assuming the medium to be laterally slowly varying. The plot on top clearly shows the differences in the transitions which have a drastic effect on the behavior of the shot records. The shot records display differing AVO and frequency characteristics.

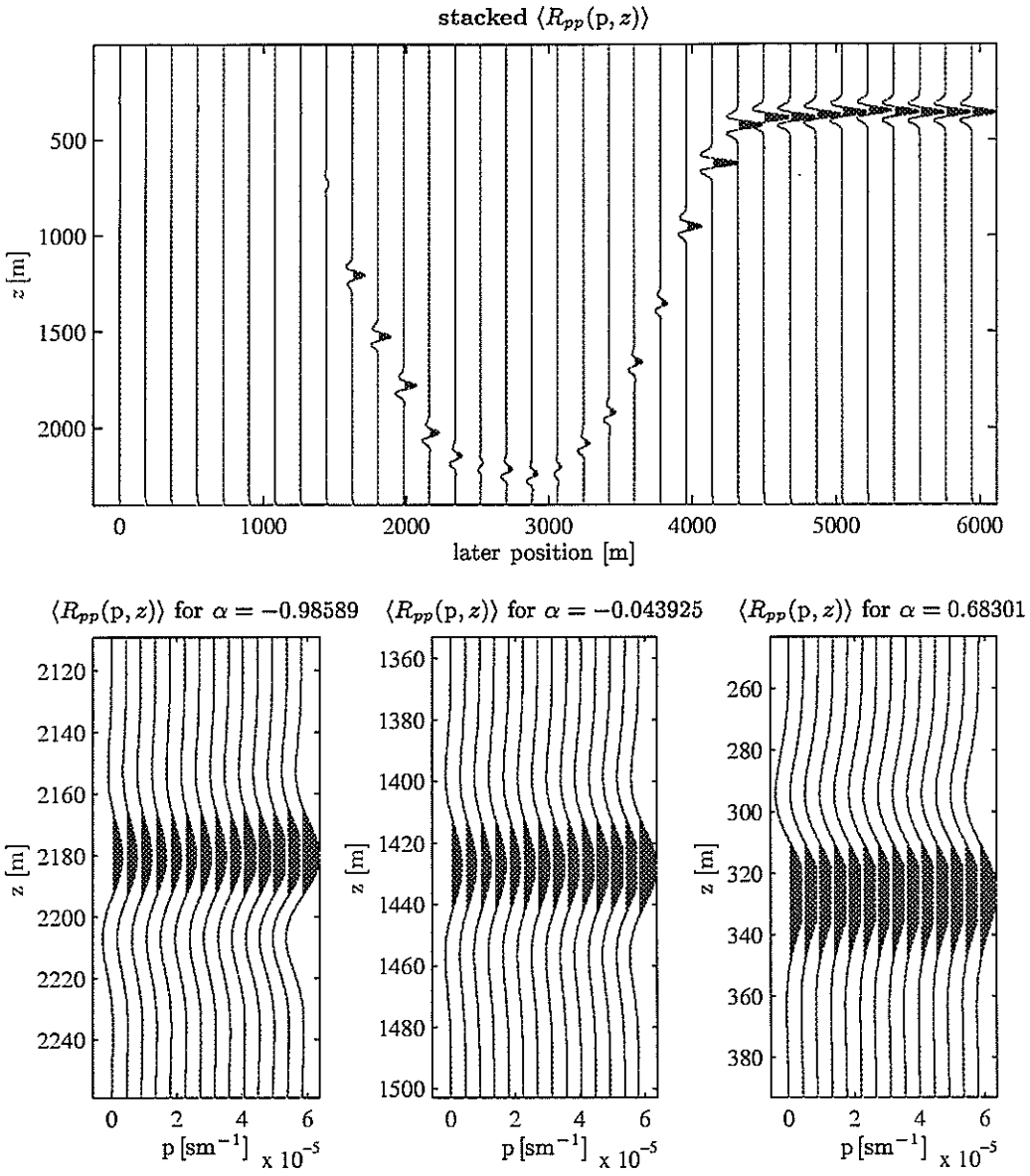

Figure 12: Imaged reflectivity data obtained after migration of the shot records generated from the model depicted in Figure 11 (top). The post-stack data is depicted on the top for all shot locations. Migrated reflection gathers corresponding to the shot records of Figure 11 (bottom) are depicted in the lower column as well. Again, notice the differences in appearance as a function of the transition's order, α. As the transition becomes less sharp (larger α) the amplitudes of the reflectivity decrease, explaining the bad visibility of the transition on the left-hand side of the model.

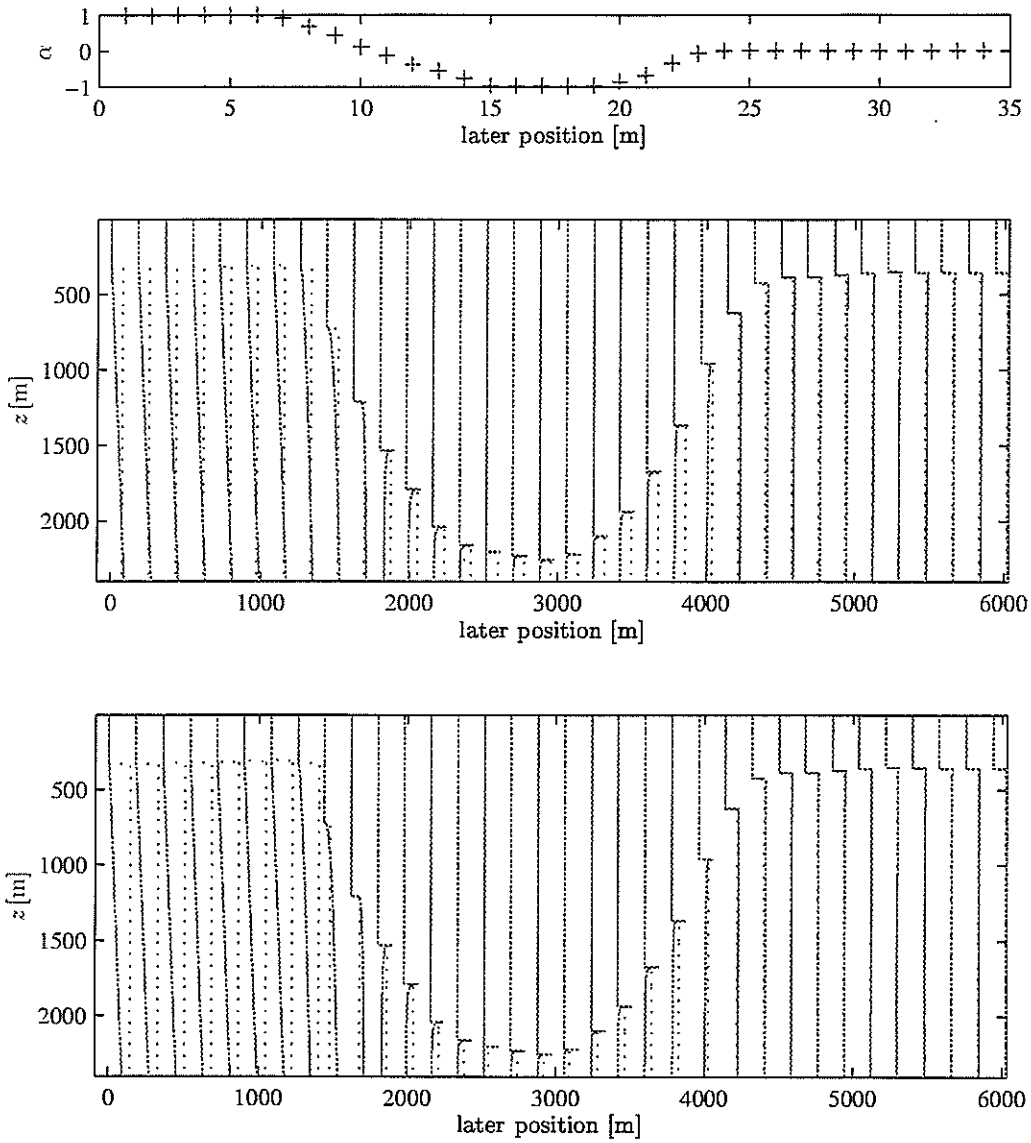

Figure 13: Zoeppritz inversion on the data generated from the model in Figure 11. On the top the lateral variations in the sharpness (α). In the middle the reconstructed (dashed) and original (solid lines) acoustic impedance. On the bottom the same for the compressional wavespeed fluctuations. Notice the exceeding overestimation of the c_p fluctuations as the sharpness (α) increases. This effect is known as "tuning" by a "thin" layer.

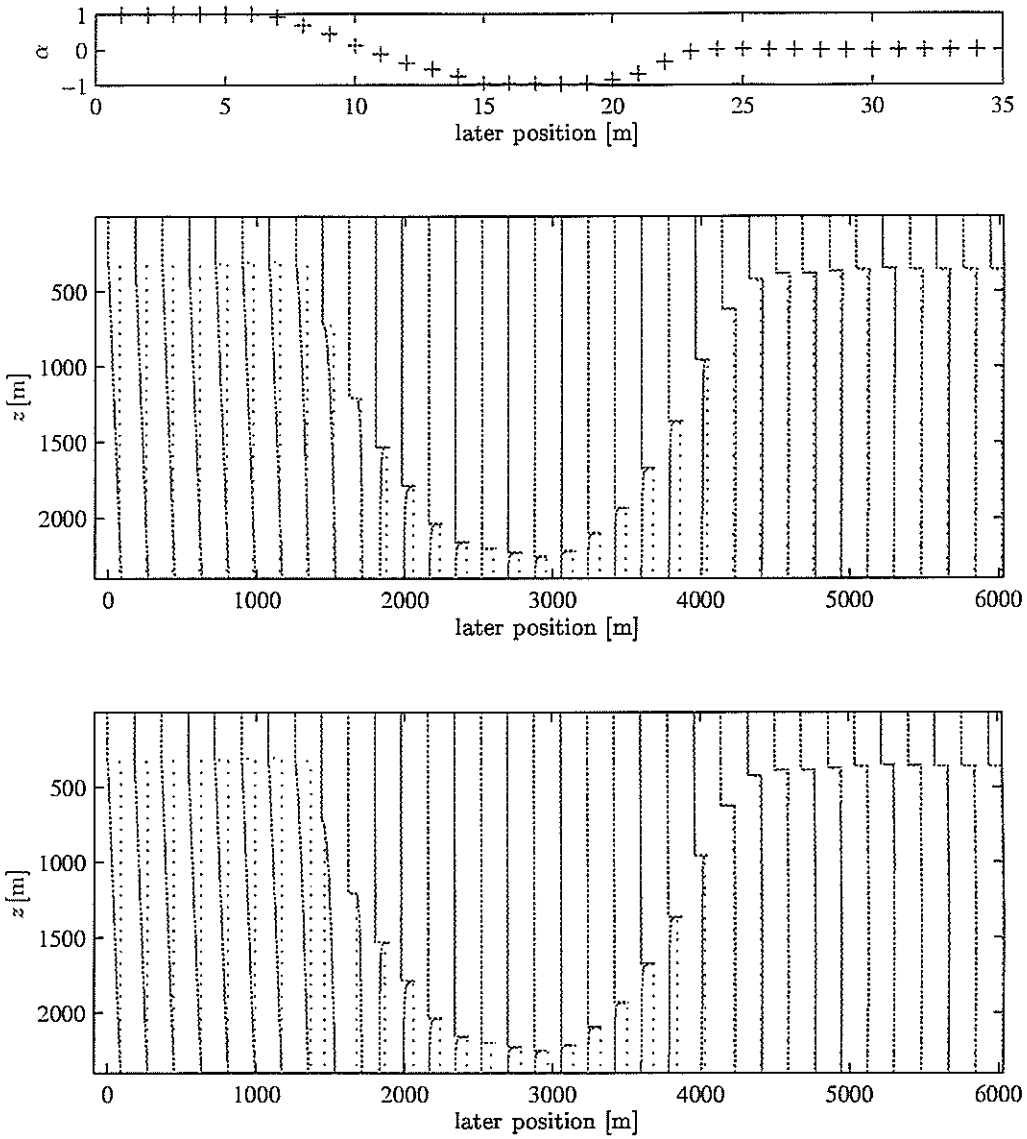

Figure 14: Renormalized Zoeppritz inversion on the data generated from the model in Figure 11. On the top the lateral variations in the sharpness (α) are depicted. In the middle the reconstructed (dashed) and original (solid lines) acoustic impedance. On the bottom the same for the compressional wavespeed fluctuations. Notice the much improved estimates for the c_p fluctuations especially when the sharpness (α) increases. Apparent "tuning" effects are to a large degree removed by this procedure.

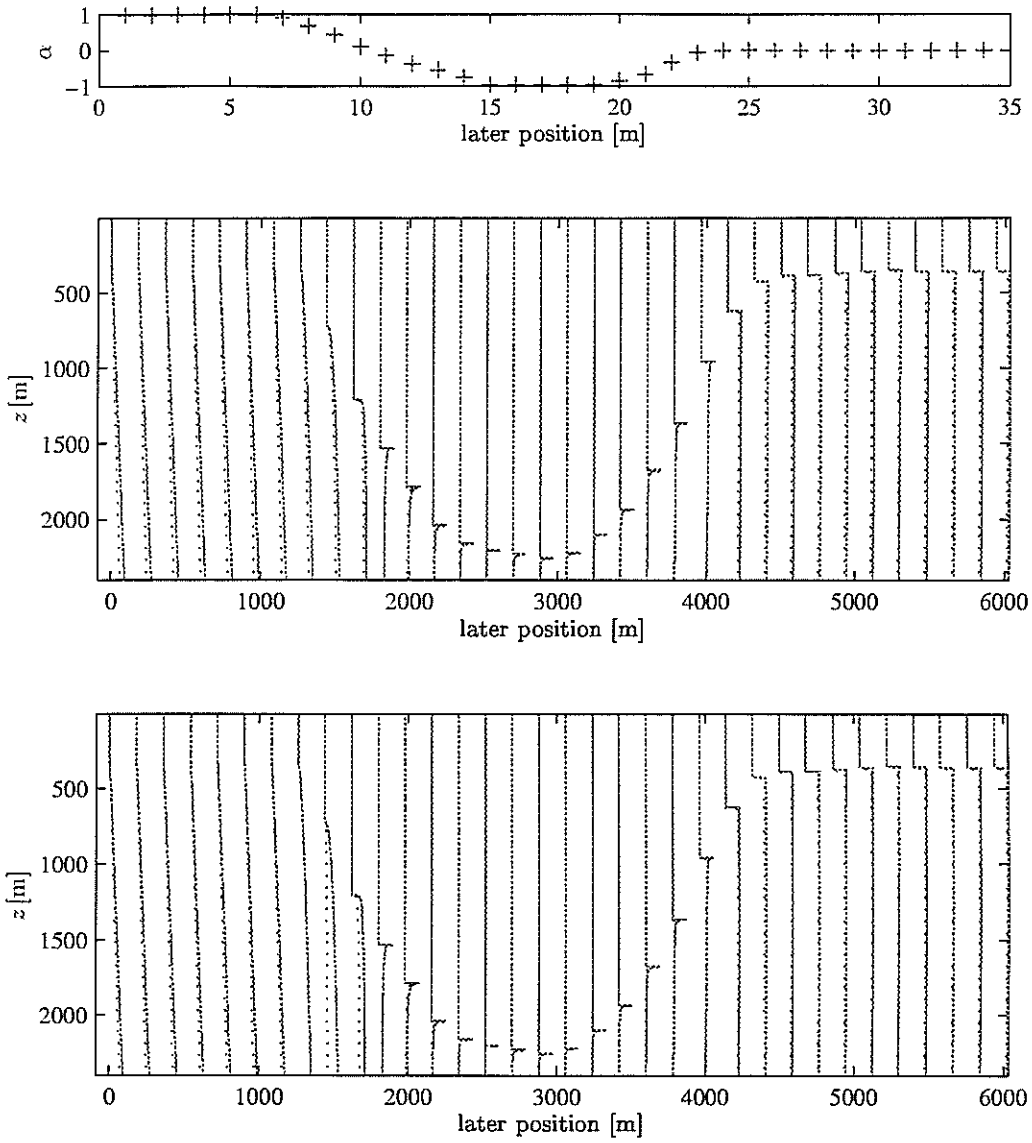

Figure 15: Same as Figure 14 but now incorporating sharpness information in the transition reconstruction as well. The reconstruction is based on equation 42 and yields a very nice reconstruction for almost all the different transitions.